POLITECNICO DI TORINO
Repository ISTITUZIONALE

Detecting riming in stratiform clouds using EarthCARE Doppler observations

Original
Detecting riming in stratiform clouds using EarthCARE Doppler observations / Kim, J., Kollias, P., Puigdomènech Treserras, B., Battaglia, A., Qu, Z., Nguyen, C.. - In: ATMOSPHERIC MEASUREMENT TECHNIQUES. PAPERS IN OPEN DISCUSSION.. - ISSN 1867-8610. - (2026). [10.5194/egusphere-2026-6312]

Availability:
This version is available at: 11583/3018286 since: 2026-11-22T18:02:15Z

Publisher:
EGU

Published
DOI:10.5194/egusphere-2026-6312

Terms of use:

This article is made available under terms and conditions as specified in the corresponding bibliographic description in the repository

Publisher copyright

(Article begins on next page)

28 November 2026

https://doi.org/10.5194/egusphere-2026-6312
Preprint. Discussion started: 23 October 2026
© Author(s) 2026. CC BY 4.0 License.

Detecting riming in stratiform clouds using EarthCARE Doppler observations

Jiseob Kim[1], Pavlos Kollias[1,2], Bernat Puigdomènech Treserras[1], Alessandro Battaglia[3], Zhipeng Qu[4], Cuong Nguyen[5]

[1]Department of Atmospheric and Oceanic Sciences, McGill University, Montréal, QC, Canada
[2]School of Marine and Atmospheric Sciences, Stony Brook University, Stony Brook, NY, USA
[3]Department of Environment, Land and Infrastructure Engineering (DIATI), Politecnico di Torino, Torino, Italy
[4]Environmental Research and Modelling Directorate, Environment and Climate Change Canada, Toronto, ON, Canada
[5]Flight Research Laboratory, National Research Council Canada, Ottawa, ON, Canada

Correspondence to: Jiseob Kim (jiseob.kim@mcgill.ca)

Abstract. The EarthCARE Cloud Profiling Radar (CPR), the first Doppler cloud radar in space, provides near-global Doppler velocity observations from which hydrometeor sedimentation velocity can be retrieved, creating a new opportunity to identify riming in clouds. Riming increases the density and fall speed of ice particles as supercooled liquid water (SLW) droplets freeze onto their surfaces, influencing cloud evolution and precipitation. Yet where riming occurs has remained largely beyond satellite observations. We introduce a method for detecting riming in stratiform clouds from sharp downward increases in hydrometeor sedimentation velocity. The detection threshold is derived from ice and snow gates where the Atmospheric Lidar (ATLID) signal remains unextinguished and no SLW is detected, and marks an acceleration rarely produced by vapor deposition and aggregation alone. The criterion requires a downward gradient of at least 0.4 m s^{-1} km^{-1} sustained over a minimum vertical distance of 300 m. In shallow mixed-phase clouds over ocean, detections concentrate within the independently estimated SLW layer and become more frequent as the SLW amount increases. Riming detection frequency often exceeds 50% within the layer once SLW path surpasses about 200 g m^{-2}. During a coordinated aircraft underflight, rimed particles were visually identified within and below detected riming regions, while a region dominated by unrimed crystals and aggregates showed little detected riming. These aircraft observations consistently support the interpretation that the detected signatures correspond to riming. The resulting observations provide a new satellite-based constraint on the occurrence of riming and its representation in weather and climate models.

1 Introduction

Clouds regulate both Earth's radiation budget and the hydrological cycle, yet they remain one of the dominant sources of uncertainty in weather and climate models (Bony et al., 2015; Ceppi et al., 2017; Morrison et al., 2020). This challenge is particularly pronounced in mixed-phase clouds (Cesana et al., 2015; Hofer et al., 2024; Frostenberg et al., 2026), where ice and supercooled liquid water (SLW) coexist under thermodynamically metastable conditions below 0 °C. In mixed-phase clouds, the partitioning between liquid and ice strongly influences cloud optical depth through the contrasting sizes and number

https://doi.org/10.5194/egusphere-2026-6312
Preprint. Discussion started: 23 October 2026
© Author(s) 2026. CC BY 4.0 License.

concentrations of droplets and ice crystals, while the transfer of water to growing ice particles promotes precipitation development (Korolev et al., 2017; Forster et al., 2021). Riming is an efficient mechanism for transferring cloud water into precipitating ice.

During riming, supercooled liquid droplets collide with and freeze onto ice crystals, yielding denser and heavier particles that precipitate out more efficiently (Locatelli and Hobbs, 1974). Numerical simulations have shown that the degree of riming affects particle fall speeds and horizontal transport, which in turn alter the intensity, timing, and location of surface precipitation (Morrison et al., 2015; DeLaFrance et al., 2024a). Riming also transfers SLW to ice particles, reshaping the phase partitioning of mixed-phase clouds and affecting cloud persistence and radiative effects. For example, reducing the riming rate increased liquid water path in simulations of Southern Ocean boundary layer clouds, and the same modification in a global model raised the annual mean shortwave radiation reflected to space over the Southern Ocean by up to 6 W m^{-2} (Furtado and Field, 2017). In cold-air outbreak clouds, riming can accelerate the breakup of an overcast stratocumulus deck into a broken, open-cellular cloud field through the evaporation and sublimation of precipitation below cloud base, thereby altering cloud radiative effects (Abel et al., 2017; Tornow et al., 2021; Karalis et al., 2022).

Despite its importance, riming remains poorly constrained by observations. Traditionally, it has been observed by identifying accreted rime and associated morphological features on individual ice particles sampled at the surface or by aircraft (Ono, 1969; Mosimann et al., 1994; Praz et al., 2017; Waitz et al., 2022), but the limited sampling makes it difficult to infer the distribution of riming throughout the cloud. Radar studies have probed riming through its signatures in particle scattering and fall speed. Multifrequency radar reflectivities, often interpreted with scattering models, have been used to identify riming signatures through their sensitivity to particle size and density (Kneifel et al., 2015; Leinonen and Szyrmer, 2015; Leinonen et al., 2018; Tridon et al., 2022). Doppler velocity has provided an additional constraint on particle density (Mason et al., 2018, Kneifel and Moisseev 2020), while polarimetric variables have added information on particle shape, helping distinguish riming from aggregation (Oue et al., 2021). Doppler spectra have further revealed distinct liquid and ice modes in mixed-phase clouds (Shupe et al., 2004; Luke et al., 2010), allowing changes in the ice population associated with riming to be traced through an SLW layer (Kalesse et al., 2016). Triple-frequency spectral ratios have also differentiated rimed and unrimed snow aggregates (Kneifel et al., 2016). An approach using artificial neural networks has been proposed to estimate rime mass fraction from radar reflectivity, mean Doppler velocity, spectrum edge width, and skewness (Vogl et al., 2022).

These studies demonstrate that riming (or rimed particles) can be effectively detected and characterized when multiple radar observables are available. However, the measurement requirements limit the range of observing systems to which these methods can be applied. Most of the approaches described above cannot be directly transferred to radars operating at a single frequency and polarization with only a limited set of radar moments. A simpler approach relies on Doppler velocity alone, which is sensitive to the enhanced particle fall speeds associated with riming. Kneifel and Moisseev (2020), building on Mosimann (1995), established an observational relationship between mean Doppler velocity (MDV) and rime mass fraction, allowing riming to be identified with vertically pointing radars operating at a single frequency. Ockenfuß et al. (2025) applied this relationship to identify individual riming events and characterize their vertical extent, duration, and horizontal scale.

https://doi.org/10.5194/egusphere-2026-6312
Preprint. Discussion started: 23 October 2026
© Author(s) 2026. CC BY 4.0 License.

Particle fall speed, however, depends on factors beyond the degree of riming, and the velocities of large unrimed aggregates can overlap with those of lightly rimed particles (Matrosov, 2023). The additional influence of vertical air motion calls for conservative Doppler velocity thresholds, restricting the method largely to particles with rime mass fractions above approximately 0.5, corresponding to a W-band MDV of about 1.25 m s^{-1} in the parameterization of Kneifel and Moisseev (2020). Such thresholds may therefore leave weak or incipient riming undetected.

Vertical gradients of Doppler velocity offer another view of riming by providing information on the microphysical changes that particles undergo as they fall, provided that the contribution of vertical air motion can be effectively isolated and removed. This perspective has roots in early observations linking vertical Doppler velocity changes to riming (Weiss and Hobbs, 1975) and in the broader use of vertical gradients in radar observables to investigate cloud microphysics (Schrom and Kumjian, 2016; Planat et al., 2021; Kalogeras et al., 2021; Zaremba and Rauber, 2025; Yan et al., 2025). Because riming rapidly increases particle fall speed over a relatively short vertical distance, vertical gradients can reveal riming even while the particles are still falling relatively slowly. The Earth Cloud, Aerosol and Radiation Explorer (EarthCARE; Illingworth et al., 2015; Wehr et al., 2023), launched in May 2024, offers a new opportunity to detect riming from space with the first spaceborne Doppler Cloud Profiling Radar (CPR; Kollias et al., 2018, 2022). This capability relies on the W-band reflectivity-weighted hydrometeor sedimentation velocity (V_{SED}) available for stratiform clouds in the European Space Agency (ESA) Level-2 (L2) Corrected CPR Doppler Measurements (C-CD; Kollias et al., 2023) product, derived from Doppler velocity by removing the contribution of vertical air motion (Puigdomènech Treserras et al., 2026).

We introduce a method that identifies riming in stratiform clouds from marked downward increases in V_{SED}, reflecting the rapid acceleration of sedimenting ice particles as rime mass accumulates. The method aims to identify where riming occurs, not where rimed particles are present. We first use ice and snow regions where the Atmospheric Lidar (ATLID) detects no SLW as a non-riming reference to determine the upper range of V_{SED} accelerations expected from vapor deposition and aggregation alone, and define the detection threshold accordingly. We then assess whether the detected signals are consistent with conditions favorable for riming, using independent estimates of SLW amount and vertical extent from EarthCARE measurements. This assessment is limited to shallow mixed-phase clouds over ocean, where these quantities can be more reliably estimated. We further evaluate the detected signatures using in situ aircraft observations acquired during an EarthCARE underflight, examining whether they are consistent with the presence of rimed particles. We then present the first near-global distribution of riming detection frequency in stratiform clouds using EarthCARE observations from 2025.

2 EarthCARE Level-2 Products and Derived Quantities

We utilize the EarthCARE L2 CPR products (Kollias et al., 2023) to identify riming. EarthCARE L2 products are developed separately by the ESA and the Japan Aerospace Exploration Agency (JAXA) (Wehr et al., 2023; Eisinger et al., 2024). This study uses ESA data products; consequently, the results are specific to this processing chain. The study encompasses global observations spanning 83°S to 83°N from January to December 2025. Although EarthCARE data collection officially

https://doi.org/10.5194/egusphere-2026-6312
Preprint. Discussion started: 23 October 2026
© Author(s) 2026. CC BY 4.0 License.

commenced in June 2024, observations prior to 5 December 2024 were affected by a technical issue related to an imbalance in the CPR's in-phase/quadrature (I/Q) channels. According to the JAXA release notes (JAXA, 2025), this issue impacted the accuracy of the Level-1 products on which the L2 retrievals are based. To ensure data quality and maintain a consistent one-year analysis period, this study uses observations collected during 2025 only.

2.1 Primary CPR Variables: Reflectivity and Sedimentation Velocity

The L2 radar reflectivity (Z) is obtained from the CPR Feature Mask and Reflectivity (C-FMR) product (baseline BD), which applies feature masking, gaseous attenuation correction, and calibration to the raw reflectivity, although it does not account for attenuation by liquid water (Kollias et al., 2023). The native CPR sampling is 500 m along track, but the L2 products have a 1-km along-track spacing. In the vertical, the 500-m pulse length determines the physical resolution, while the data are oversampled at 100-m intervals. Its sensitivity is approximately −35 dBZ in the troposphere. Near the surface, CPR measurements are affected by surface clutter, which typically contaminates the lowest about 500–600 m over the ocean (Xu et al., 2026). Validation against ground-based radar systems has shown that the L2 reflectivity is well calibrated and unbiased (Feuillard et al., 2026).

The primary variable used for riming detection is the sedimentation velocity best estimate (hereafter V_{SED}), provided in the C-CD product (baseline BD). This estimate represents the W-band reflectivity-weighted fall speed of hydrometeors. To obtain this, the CPR first estimates raw Doppler velocity based on the phase shift between successive backscattered pulses. Although the radar reports values every 100 m, each estimate represents a reflectivity-weighted average over the 500-m pulse length rather than an independent 100-m layer.

The C-CD algorithm corrects several known sources of instrumental error, including antenna mispointing, non-uniform beam filling effects, and velocity folding (Kollias et al., 2023; Puigdomènech Treserras et al., 2025). At present, velocity unfolding is applied only to rain. To suppress random noise, the real and imaginary parts of the pulse-pair covariance are spatially averaged over a 4-km along-track and 500-m vertical window. Consequently, adjacent pixels do not represent independent measurements, as each reported value reflects spatial averaging in both dimensions. For ice clouds, the Doppler velocity uncertainty is estimated at approximately 0.5 m s^{-1} (Kollias et al., 2023), while the bias is reported to be near zero (Kim et al., 2025). Under low signal-to-noise ratio (SNR) conditions, Doppler velocity uncertainty increases substantially. Accordingly, Doppler measurements are considered reliable only where reflectivities exceed −21 dBZ, a threshold at which the SNR is approximately 0 dB.

The observed Doppler velocity (V_D) is the sum of the hydrometeor sedimentation velocity (V_{SED}), vertical air motion (V_{AIR}), and measurement error (ε):

$$V_D = V_{SED} + V_{AIR} + \varepsilon. \quad (1)$$

https://doi.org/10.5194/egusphere-2026-6312
Preprint. Discussion started: 23 October 2026
© Author(s) 2026. CC BY 4.0 License.

Following standard radar convention, velocity is defined as positive for motion away from the radar; therefore, falling particles have positive V_{SED}. The key assumption used to retrieve V_{SED} is that V_{AIR} and ε average to zero over sufficiently large scales within regimes of similar microphysical and thermodynamic properties. In the C-CD algorithm, these regimes are defined based on similarities in radar reflectivity and temperature (T). This approach is analogous to the established terminal fall speed–radar reflectivity–height method (Plana-Fattori et al., 2010; Protat and Williams, 2011; Kalesse and Kollias, 2013), which uses height as a proxy for temperature to account for variations in particle habit and density. For EarthCARE, the temperature information is taken from the ECMWF meteorological fields (X-MET) and, from baseline BC onward, is provided on the CPR grid through the CPR Target Classification (C-TC; Irbah et al., 2023) product (baseline BD used here).

In earlier versions of the C-CD algorithm (through baseline BC), this spatial averaging was performed by averaging Doppler velocities within a 300-m vertical window and along-track windows of varying lengths (10, 20, 30, and 40 km), selecting the smallest window that provided sufficient sampling (Kollias et al., 2023). Although effective, this approach was prone to artificial discontinuities at processing boundaries and often failed to filter out larger-scale vertical air motions, such as gravity waves with horizontal scales exceeding 40 km.

To overcome these limitations, the current algorithm (from baseline BD onward) employs a more sophisticated approach. Instead of fixed windows, it uses an adaptive weighting kernel that determines the relative contribution of each observation based on its spatial proximity (up to 250 km along-track), variability, and similarity in the Z–T space, while also accounting for correlations between observations (detailed in Puigdomènech Treserras et al., 2026). This provides a continuous and more robust estimation of V_{SED}. Retrievals are restricted to gates with valid reflectivity and Doppler measurements and screened to exclude regions affected by convection. In relatively quiescent stratiform regimes, this method achieves a retrieval uncertainty of 0.1–0.2 m s^{-1}. The C-CD product also provides an uncertainty estimate and, separately, a measure of V_{SED} variability indicating the spread of the velocity samples averaged for each V_{SED} estimate.

The retrieved V_{SED} therefore provides an estimate of particle fall speed, reflecting the characteristic size and density of the hydrometeor population as captured by CPR. To account for changes in air density, all V_{SED} values are corrected and referred to a given reference density following Foote and du Toit (1969), as described in Appendix A.

2.2 Estimation of Vertical Gradients

The vertical gradients of Z and V_{SED} reflect microphysical changes along the direction of particle fall that are not readily apparent from the absolute fields alone (Yan et al., 2025). In this study, we introduce s as a downward vertical coordinate that increases toward the surface to align the analysis with the falling hydrometeors. The gradients of Z (denoted G_Z, dBZ km^{-1}) and V_{SED} (denoted G_V, m s^{-1} km^{-1}) are defined as the slopes of linear regressions of the respective variables against s over a specified vertical window. The fitted slope is assigned to the center gate of the window. Under this convention, a positive gradient indicates a downward increase (e.g., acceleration for V_{SED}), while a negative gradient represents a decrease.

The term “acceleration” is used here for convenience, but it should be noted that it does not represent the actual acceleration of individual particles during their descent. The radar observes hydrometeors at different heights but does not track individual

https://doi.org/10.5194/egusphere-2026-6312
Preprint. Discussion started: 23 October 2026
© Author(s) 2026. CC BY 4.0 License.

particles as they fall. A downward increase in V_{SED} therefore reflects differences in the particle population sampled at different heights. Differential sedimentation can cause particles with higher fall speeds to reach lower levels sooner, while slower particles lag behind or are more readily retained aloft. Local particle production and horizontal advection can further modify the sampled particle population. Studies using high-resolution ground-based radars have shown that, when strong wind shear produces slanted fall streaks, vertical gradients can reflect advection more strongly than microphysical evolution (Planat et al., 2021). However, the coarser CPR resolution and broader spatial averaging used in the V_{SED} retrieval (up to 250 km horizontally) are expected to suppress much of the small-scale variability.

The regression window length is determined from the vertical autocorrelation of V_{SED}, which exhibits stronger gate-to-gate dependence than Z. The mean autocorrelation between adjacent V_{SED} samples (i.e., 100 m apart) is approximately 0.73 (Appendix B). Using the mean autocorrelation function (ACF) to estimate the effective sample size (see Fig. B2), we found that an 11-gate window (i.e., 1 km between the outer gate centers) corresponds to about three independent samples. This was adopted as the minimum window length required to retain one residual degree of freedom (DOF) in the linear regression. Where a full 11-gate window is not available, such as near cloud boundaries or other vertically limited regions, the regression window is reduced stepwise and allowed to become asymmetric to preserve data coverage. A minimum of seven valid gates is required, as smaller windows reduce the effective sample size below two and thus do not provide sufficient DOF for a statistically meaningful slope estimate. To maintain consistency, the same regression window is applied to G_Z.

2.3 Auxiliary Information for Evaluating Riming Detection Reliability

The aim of this study is to identify riming using CPR observations alone. However, in the absence of a dedicated reference product for riming, the CPR-based riming signatures cannot be evaluated through direct validation against a reference dataset. We therefore use independent physical constraints to evaluate whether the detected signatures are consistent with conditions favorable for riming. Because riming requires the coexistence of ice and SLW, the occurrence and amount of SLW provide independent constraints for evaluating the detected signatures. For example, the presence of a sufficient amount of SLW helps assess whether the environmental conditions support riming, while its absence allows us to assess potential false detections in the algorithm. We use the ATLID–CPR Target Classification (AC-TC; Irbah et al., 2023) product to identify SLW occurrence and incorporate path-integrated attenuation (PIA) as a proxy for liquid water amount.

2.3.1 ATLID-Based Detection of Supercooled Liquid Water

The AC-TC product provides a synergistic target classification by combining independent CPR and ATLID classifications. SLW identification relies exclusively on ATLID, as high concentrations of small liquid droplets produce strong backscatter and relatively low depolarization in the ATLID signal, while these droplets are typically too small to be detected by the CPR. However, since the ATLID signal is rapidly extinguished in liquid, it mainly constrains the uppermost SLW layer top and does not provide information on the layer depth or amount. We define the SLW top as the highest vertical gate among those identified as containing SLW, provided that the lidar view is not obscured by an overlying SLW or optically thick ice layer.

https://doi.org/10.5194/egusphere-2026-6312
Preprint. Discussion started: 23 October 2026
© Author(s) 2026. CC BY 4.0 License.

To quantify false detections, we define an "ice/snow-only" reference population consisting of ice targets (including snow) where the ATLID signal remains unextinguished and no SLW is detected.

2.3.2 Path-Integrated Attenuation (PIA) and Proxy Liquid Water Path

To constrain the amount of SLW, we utilize the PIA from the C-FMR product (Sasikumar et al., 2026), which quantifies the cumulative CPR signal loss due to hydrometeors. Operationally, this value is estimated via the surface reference technique (SRT). The SRT calculates the departure of the observed normalized radar cross-section from the expected clear-sky surface return over oceanic regions, after subtracting the contribution of gaseous attenuation. PIA uncertainty depends on surface wind conditions and clear-sky reference sampling, but is typically below 1 dB (Sasikumar et al., 2026).

At the W-band frequency, attenuation in mixed-phase clouds is generally dominated by liquid water because its absorption is much stronger than that of ice. Consequently, for cloud profiles residing entirely at sub-zero temperatures, the observed signal loss is predominantly driven by absorption due to SLW, whereas the ice phase contribution, occurring mainly through scattering, is typically much smaller (Tridon et al., 2020). Although scattering attenuation by ice can become non-negligible for large snowflakes or heavily rimed particles, estimating its magnitude is highly sensitive to particle size, mass, density, and habit, making a robust correction difficult. To minimize these uncertainties, we restrict the liquid water path (LWP) estimation specifically to single-layer, low-level clouds with cloud top heights below 2.5 km over ocean.

The persistence of such low-level mixed-phase clouds (hereafter LLMPCs) generally depends on a sustained supply of SLW, whereas ice particles rapidly precipitate out if that liquid source is removed. As a result, the water mass is typically dominated by liquid water rather than ice (Shupe et al., 2008), a condition under which Tridon et al. (2020) showed that PIA can provide a reasonable proxy for LWP. Moreover, SLW is typically concentrated near cloud top owing to cloud top radiative cooling and turbulence (Yan et al., 2025). This concentration of liquid near the top facilitates a more representative temperature estimate, which is essential for assigning the appropriate mass absorption coefficient.

In this study, we use PIA as a proxy for supercooled liquid water path (SLWP) in atmospheric columns entirely below 0 °C, following the linear relationship:

$$PIA \approx \alpha(T) \cdot SLWP, \quad (2)$$

where α (dB kg^{-1} m^2) is the mass absorption coefficient at temperature T. We adopt the liquid water absorption model from Turner et al. (2016), which is specifically optimized for cold, mixed-phase environments and maintains an uncertainty below 15% for temperatures as low as −32 °C. To account for the temperature dependence of α, we utilize the mean temperature from the five CPR gates (~500 m) immediately below the ATLID-detected SLW top.

https://doi.org/10.5194/egusphere-2026-6312
Preprint. Discussion started: 23 October 2026
© Author(s) 2026. CC BY 4.0 License.

2.3.3 Estimation of Effective SLW Thickness

We estimate an effective SLW layer thickness assuming adiabatic liquid water content (LWC). Within this layer, the LWC can be approximated as increasing linearly with height above the liquid base,

$$LWC(z) = f_{ad}\Gamma_{ad}z, \quad (3)$$

where z is the height above the liquid base, f_{ad} is the degree of adiabaticity, and Γ_{ad} is the adiabatic rate of increase of LWC with height. The value of Γ_{ad} depends on temperature and pressure (p) and can be expressed as

$$\Gamma_{ad}(T,p) = \rho_a(T,p)\frac{c_p}{L_v}[\Gamma_d - \Gamma_m(T,p)], \quad (4)$$

where ρ_a is the air density, c_p is the specific heat of dry air at constant pressure, L_v is the latent heat of vaporization, and Γ_d and Γ_m are the dry and moist adiabatic lapse rates, respectively. Over the shallow layers considered here, Γ_{ad} is assumed to be vertically constant (denoted by $< \Gamma_{ad} >$) and is computed using the mean temperature and pressure from the five CPR gates immediately below the ATLID-detected SLW top, consistent with the temperature used in the PIA-to-SLWP conversion. Integrating the linear profile from the liquid base to the top of the liquid layer gives

$$SLWP = \int_0^{h_{SLW}} LWC(z)dz = \frac{1}{2}f_{ad} < \Gamma_{ad} > h_{SLW}^2, \quad (5)$$

and therefore

$$h_{SLW} = \left(\frac{2SLWP}{f_{ad}<\Gamma_{ad}>}\right)^{1/2}. \quad (6)$$

We adopt f_{ad} = 0.85, representing modest subadiabaticity typical of stratiform clouds. Although processes such as liquid depletion via ice precipitation and cloud-top entrainment can further reduce adiabaticity in mixed-phase environments (Klein et al., 2009), sensitivity tests varying f_{ad} from 0.6 to 1.0 indicate that this assumption changes h_{SLW} by less than 20% relative to the default value. The estimated liquid base height is obtained by subtracting h_{SLW} from the ATLID-detected SLW top height.

2.4 Aircraft Observations during ECALOT

For an independent case-study evaluation of the CPR-based riming detection, we use observations from Flight 7 of the EarthCARE Commissioning Cal/Val Campaign in Ottawa (ECALOT; Qu et al., 2026), conducted on 25 March 2025 with the National Research Council Canada (NRC) Convair-580 research aircraft. The primary instruments used in this study are the

https://doi.org/10.5194/egusphere-2026-6312
Preprint. Discussion started: 23 October 2026
© Author(s) 2026. CC BY 4.0 License.

NRC airborne W-band radar (NAW), the Cloud Particle Imager (CPI), the 2-Dimensional Stereo (2D-S) and High Volume Particle Spectrometer-4 (HVPS-4) optical array probes (OAPs), and the Nevzorov probe. Operating at the same frequency as the EarthCARE CPR, the NAW provides vertically pointing reflectivity and Doppler velocity measurements above and below the aircraft during this flight, with a nominal beamwidth of about 0.75°, a range resolution of 75 m, and a minimum detectable signal of −30 dBZ at 1 km range (Wolde et al., 2019; Nguyen et al., 2022). The closest usable NAW range gate is approximately 350 m from the aircraft. Because corrections for aircraft motion and attitude are still under development, the airborne Doppler velocities are used only for qualitative comparison with the EarthCARE observations.

In situ microphysical measurements are used to quantify the liquid and ice-phase properties along the flight track. LWC is derived from the Nevzorov probe because the cloud droplet probe (CDP) measurements were unreliable during this flight. The Nevzorov instrument determines bulk LWC through constant temperature hot-wire measurements (Korolev et al., 1998). While the LWC uncertainty is typically below 20% for pure liquid clouds with droplet diameters between 5 and 50 μm, it can increase significantly beyond this level in mixed-phase environments. Ice water content (IWC) is derived from the composite OAP size distribution based on 2D-S and HVPS-4 measurements using an empirical mass-size relationship (Brown and Francis, 1995), with an estimated uncertainty of 20−40%. High-resolution CPI images (15−2000 μm) are used qualitatively to identify the presence of SLW droplets as well as rimed ice particles and unrimed ice particles.

3 CPR-Based Riming Detection

Figure 1 summarizes the CPR-based riming detection procedure. After preprocessing the CPR observations and calculating the vertical gradients, a detection threshold is derived from the ice/snow-only reference population to identify accelerations rarely produced by unrimed ice growth. The resulting riming detections are then evaluated using independent estimates of SLW occurrence and amount in LLMPCs.

https://doi.org/10.5194/egusphere-2026-6312
Preprint. Discussion started: 23 October 2026
© Author(s) 2026. CC BY 4.0 License.

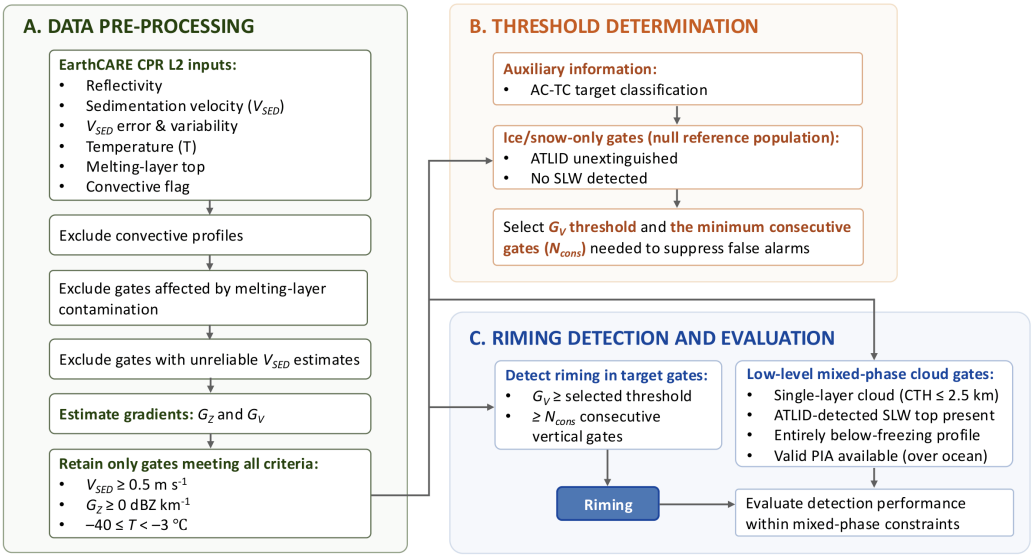


Figure 1: Overview of the CPR-based riming detection methodology, including data preprocessing, threshold determination, riming detection, and independent evaluation using SLW observations.

3.1 Data Preprocessing

Preprocessing begins by restricting the dataset to stratiform cloud regimes. Although V_{SED} retrievals are not attempted in convective regions, we also exclude the entire profile if convection is identified to avoid including vertically adjacent cloud regions that may still be influenced by convective motions. This screening is implemented using the simplified convective classification provided in the C-TC product. The convective classes include deep convective cloud, dynamic convective core, and heavy mixed-phase precipitation.

Even within these stratiform regimes, additional precautions are taken to avoid spillover effects from the melting layer. Because melting particles fall substantially faster than ice particles (often more than twice as fast; Puigdomènech Treserras et al., 2026), a CPR pulse length that straddles the phase transition can artificially elevate V_{SED} in the ice layer immediately above the melting layer top. This contamination is particularly problematic for the present analysis, as it can introduce spurious positive gradients just above the melting layer that are unrelated to riming. To prevent such effects, we exclude the five gates above whichever is higher: the 0 °C level or the melting layer top identified from the C-TC product. Approximately 90% of the excluded gates occur at temperatures warmer than −3 °C.

An additional screening step is applied based on the V_{SED} error and variability provided in the C-CD product. This gate-by-gate filter helps screen out potentially unreliable retrievals affected by residual dynamical motions—such as gravity waves, localized turbulence, or weaker convective elements—that may have bypassed the initial screening. To ensure the reliability of riming identification, we require the V_{SED} error and variability to be below 0.25 m s^{-1} and 0.6 m s^{-1}, respectively, following

https://doi.org/10.5194/egusphere-2026-6312
Preprint. Discussion started: 23 October 2026
© Author(s) 2026. CC BY 4.0 License.

the recommended limits for reliable ice V_{SED} retrievals (Puigdomènech Treserras et al., 2026). Following this screening, the vertical gradients (G_Z and G_V) are calculated as described in Sect. 2.2.

Riming detection is further restricted to gates with $V_{SED} \geq 0.5$ m s^{-1} to reduce the influence of vertically smeared gradients in very weak sedimentation regimes. Temperature constraints further restrict the dataset used for riming detection. The lower temperature limit is set at −40 °C, as riming requires SLW, which is unlikely to persist at temperatures colder than −40 °C. The upper temperature limit is effectively set by the melting layer screening. Because this screening removes most gates warmer than −3 °C, riming detection is effectively limited to temperatures below approximately −3 °C. Additionally, only regions with $G_Z \geq 0$ dBZ km^{-1} are retained. In the stratiform ice clouds considered here, positive G_Z signifies particle growth, whereas negative G_Z is primarily interpreted as a signature of sublimation (Yan et al., 2025). Collectively, these conditions define the final set of gates (hereafter, the targeted echoes) used for riming detection.

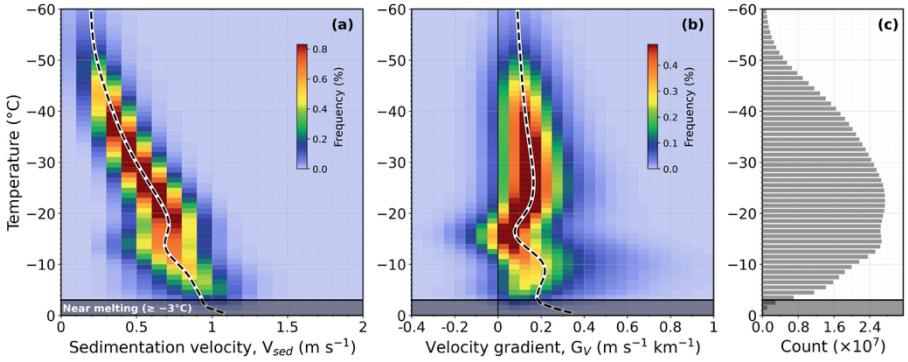


Figure 2: Joint distributions of EarthCARE CPR (a) sedimentation velocity (V_{SED}) and (b) its vertical gradient (G_V) against temperature for stratiform ice clouds where reflectivity increases downward. One year of data from January to December 2025 is used. Panel (c) shows the number of samples in each temperature bin. The dashed black lines represent the mean values at each temperature bin. The shaded area warmer than −3 °C indicates the region excluded to avoid melting layer contamination.

Figure 2 illustrates the resulting climatology of V_{SED} and G_V as a function of temperature in stratiform clouds using the subset of gates defined by the preprocessing steps, with the temperature range extended to −60 °C to provide broader thermodynamic context. The overall increase in V_{SED} with warming temperatures reflects the statistical mean of ice growth processes dominant across various stratiform cloud regimes. This trend is consistent with the progressive increase in particle size and mass typically driven by vapor deposition and aggregation. A notable exception occurs within the dendritic growth zone (DGZ; approximately −18 to −12 °C), where mean V_{SED} exhibits a slight decrease, reaching a minimum around −14 °C. Correspondingly, G_V drops sharply, with an increased occurrence of negative gradients (i.e., deceleration). Consistent with previous ground-based radar studies (von Terzi et al., 2022; Mammatt et al., 2026), this behavior is commonly attributed to the efficient growth of planar and/or dendritic ice particles favored within this specific temperature range and their development into fluffy aggregates. These particles increase their cross-sectional area more rapidly than mass, leading to enhanced aerodynamic drag. Although this DGZ-related deceleration is an interesting microphysical feature, its interpretation is beyond the scope of the study.

https://doi.org/10.5194/egusphere-2026-6312
Preprint. Discussion started: 23 October 2026
© Author(s) 2026. CC BY 4.0 License.

3.2 Threshold Determination

Determining an appropriate gradient threshold for distinguishing riming from other ice growth processes is an important step in riming detection. Riming is expected to produce a rapid increase in fall speed, as it is more directly associated with an increase in particle density. While aggregation efficiently increases particle size, it typically leads to a more modest increase in fall speed or can even result in a decline, owing to a concomitant decrease in effective density as particles grow larger and more porous (Karrer et al., 2020; DeLaFrance et al., 2024b; Kötsche et al., 2026). Accordingly, G_V is used as the primary variable for riming detection. In contrast, because both riming and aggregation can produce strong increases in reflectivity, G_Z is used solely to identify where ice growth occurs.

To isolate the G_V signatures unique to riming, we examine the background G_V distribution using the pure ice-phase gates defined in Sect. 2.3.1. Because these regions are devoid of SLW, they provide a null reference population that defines the upper range of G_V values expected from vapor deposition and aggregation alone. The G_V threshold is therefore selected from the upper tail of this non-riming distribution to minimize false detections.

Figure 3 presents a representative stratiform ice cloud observed over the Bering Sea on 1 September 2025 that is used to illustrate the threshold determination. The dominant cloud spans a relatively deep layer of nearly 6–7 km, extending from cloud tops near the −50 °C level to a base that dissipates close to the 0 °C isotherm (Fig. 3a). Within this region, V_{SED} (available only where $Z \geq -21$ dBZ) increases progressively from the highest retrieved levels toward the cloud base, from approximately 0.3 to 1.0 m s^{-1} (Fig. 3b). Overall, the observed V_{SED} follows the climatological median values as a function of temperature shown in Fig. 2a.

The corresponding vertical gradients of reflectivity and sedimentation velocity are shown in Figs. 3c and 3d, respectively. Apart from a shallow cloud near 160 km along track, no melting layer is observed in this case. Following the preprocessing procedure described in Sect. 3.1, the five gates immediately above the 0 °C isotherm are excluded from the gradient calculations. Across most of the cloud, reflectivity and sedimentation velocity increase downward as ice particles grow during their descent. In the lower part of the cloud, however, this trend begins to reverse, probably reflecting a rapid depletion of ice particles due to sublimation. The change is more evident in the reflectivity gradient than in the sedimentation velocity gradient because preferential sublimation of smaller ice particles leaves behind a population increasingly dominated by larger particles, allowing sedimentation velocity to continue increasing even as reflectivity decreases.

https://doi.org/10.5194/egusphere-2026-6312
Preprint. Discussion started: 23 October 2026
© Author(s) 2026. CC BY 4.0 License.

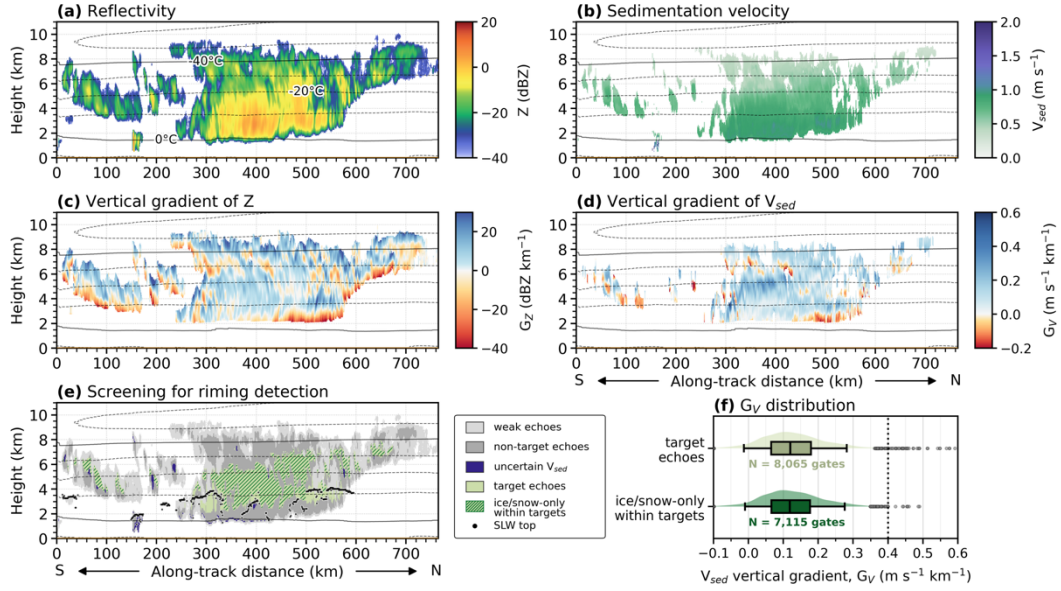


Figure 3: Example of a cloud scene observed by EarthCARE over the Bering Sea on 1 September 2025 (Orbit/Frame ID: 07167B). Panels (a)–(d) show reflectivity, sedimentation velocity, the vertical gradient of reflectivity, and the vertical gradient of sedimentation velocity, respectively. Isotherms at 10 °C intervals are overlaid in panels (a)–(e). Panel (e) shows the target gates after preprocessing for riming detection (pale green shading), from which an ice/snow-only (green hatching) subset is additionally identified. Black dots in panel (e) mark the ATLID-detected supercooled liquid water (SLW) top. Panel (f) shows the G_V distributions for the targeted echoes and the ice/snow-only subset. Boxes indicate the interquartile range with the median, whiskers span the 5th–95th percentiles, and half violins are limited to the 1st–99th percentiles. Open circles indicate values outside this range.

Figure 3e summarizes the preprocessing procedure and the resulting targeted echoes used for riming detection. The remaining gates constitute the ice/snow-only reference population used for threshold determination after excluding regions affected by convection, melting, sublimation, low sedimentation velocity, large V_{SED} uncertainty, or uncertain SLW occurrence. The G_V distributions for the targeted echoes and the ice/snow-only subset are shown in Fig. 3f. Both are concentrated at relatively weak gradients, with median G_V close to 0.12 m s^{-1} km^{-1}. In this example, 95% of all gates lie below 0.28 m s^{-1} km^{-1} and 99% below 0.35 m s^{-1} km^{-1}. Values exceeding 0.4 m s^{-1} km^{-1} are consequently uncommon, particularly within the ice/snow-only subset, where they are limited to only a handful of outliers.

We next extend the analysis to the full year of EarthCARE observations to examine whether this distribution persists statistically (leftmost pair of boxplots in Fig. 4a). As expected, the larger sample captures a broader range of observed variability, leading to wider G_V distributions. Fewer than 1% of the ice/snow-only gates nevertheless exceed 0.4 m s^{-1} km^{-1}. This low fraction may partly reflect the rarity of riming itself. Across all targeted echoes including potential riming, however, approximately 3.5% of gates exceed the same threshold (Fig. 4b), suggesting that large gradients are particularly uncommon in the ice/snow-only subset. The distributions were then separated into four temperature intervals (remaining boxplots in Fig. 4a). Below −10 °C, fewer than 1% of the ice/snow-only gates exceed the threshold in every interval. The G_V distribution

https://doi.org/10.5194/egusphere-2026-6312
Preprint. Discussion started: 23 October 2026
© Author(s) 2026. CC BY 4.0 License.

between −20 and −10 °C shifts toward smaller values, matching the reduction already seen in Fig. 2, possibly reflecting the growth of slowly falling ice particles (e.g., planar crystals, dendrites, and their aggregates). The warmest interval (−10 to −3 °C) is the only one in which more than 1% of the ice/snow-only gates lie above 0.4 m s^{-1} km^{-1}. In this interval, the fraction rises to approximately 3%, but remains well below the nearly 10% observed in the targeted echoes (Fig. 4b). The central 50% of the ice/snow-only distribution is similar to the corresponding ranges between −40 and −20 °C, suggesting that the increase is confined to a relatively small fraction of samples. By contrast, the targeted echoes show a more pronounced shift toward larger G_V values, possibly reflecting the greater prevalence of riming at these temperatures.

Inspection of these cases shows that they occur preferentially in clouds with relatively warm tops, typically as small, isolated features near profiles where SLW is detected, as shown in Appendix C. One possibility is that the broad horizontal averaging inherent in the V_{SED} retrieval allows sedimentation signatures from nearby riming regions to influence adjacent profiles in which ATLID detects no SLW. This is particularly relevant given that the Doppler velocity itself is already averaged over a 4 km along-track window before V_{SED} is retrieved. The same problem may occur at colder temperatures, but it could be amplified in the −10 to −3 °C interval, where riming is more common and the composition of the ice/snow-only sample is more strongly shaped by ATLID sampling. ATLID is more likely to retain sensitivity to this layer in clouds with relatively warm tops, while deeper clouds with colder tops are often attenuated before reaching it, potentially increasing the representation of cloud regimes with substantial horizontal microphysical variability (e.g., congestus) in the warmest interval. Increasing the G_V threshold or adopting a stricter V_{SED} uncertainty criterion would reduce these false detections but also reduce the sensitivity to riming. We therefore adopt 0.4 m s^{-1} km^{-1} as the G_V threshold for riming detection and suppress false detections by additionally requiring at least three consecutive gates ($N_{cons} \geq 3$; Fig. 4b). With this additional constraint, the false detection rate for the null reference population falls below 0.5% over the full temperature range considered for riming detection (−40 to −3 °C). The corresponding value is approximately 2% in the warmest interval. Overall, detections that remain within the ice/snow-only subset are limited under the adopted criterion.

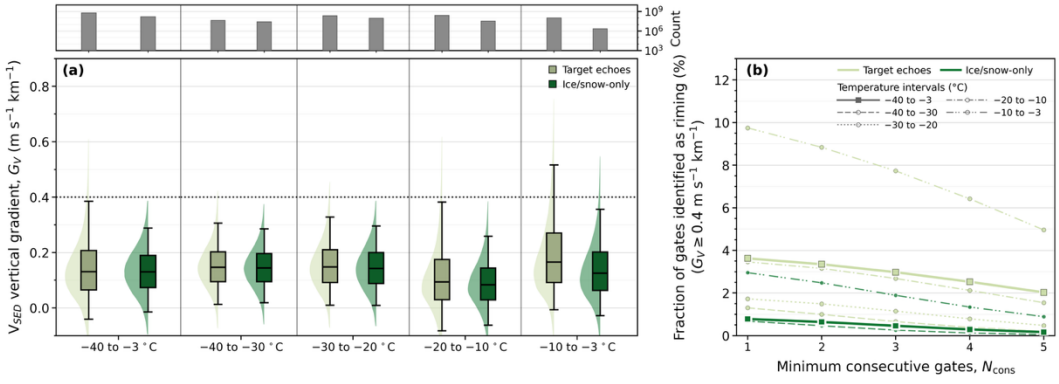


Figure 4: (a) G_V distributions for the targeted echoes used for riming detection (pale green) and the ice/snow-only subset (green) from one year of EarthCARE observations in 2025. The first pair of boxplots covers the temperature range considered for riming detection (−40 to −3 °C), and the remaining pairs correspond to four temperature intervals. Bars above indicate the number of gates. Box and half violin plots

https://doi.org/10.5194/egusphere-2026-6312
Preprint. Discussion started: 23 October 2026
© Author(s) 2026. CC BY 4.0 License.

are as in Fig. 3f. (b) Fraction of gates satisfying the $G_V \geq 0.4$ m s^{-1} km^{-1} criterion as a function of the minimum number of consecutive gates (N_{cons}) for both categories. The ice/snow-only curves for −30 to −20 °C and −20 to −10 °C are largely obscured by the −40 to −3 °C curve due to their similar values.

3.3 Riming Detection and Evaluation

We next examine whether the acceleration required to satisfy the criteria defined in the preceding section ($G_V \geq 0.4$ m s^{-1} km^{-1} and $N_{cons} \geq 3$) is consistent with conditions favorable for riming in shallow, liquid-topped mixed-phase clouds (i.e., LLMPCs). For this analysis, the LLMPC subset is defined as single-layer clouds with tops below 2.5 km that possess both ATLID-detected SLW and valid PIA-based SLWP estimates. Only profiles entirely below 0 °C are considered. These clouds provide favorable conditions for riming because of their frequent coexistence of SLW and ice particles. However, in the absence of a definitive ground truth for riming, it is difficult to rigorously define riming detection efficiency. Here, we assess whether the criteria capture the anticipated increase in frequency as the liquid water supply becomes more abundant.

Several physical processes explain why riming is expected to become more frequent as SLWP increases. In principle, in mixed-phase environments, the lower saturation vapor pressure over ice than over liquid water creates a thermodynamic tendency for vapor to deposit preferentially onto ice particles at the expense of supercooled liquid droplets. This process, known as the Wegener-Bergeron-Findeisen (WBF; Wegener, 1911; Bergeron, 1935; Findeisen, 1938) mechanism, promotes glaciation and makes the sustained coexistence of ice and SLW intrinsically unstable. When ice crystal concentrations are sufficiently high, clouds can become fully glaciated within only a few minutes to tens of minutes (Korolev and Mazin, 2003; Korolev and Milbrandt, 2022). The persistence of abundant SLW is therefore supported by continual replenishment through cloud-top radiative cooling and the associated turbulence (Morrison et al., 2012). Turbulence also helps maintain liquid saturation while enhancing collisions between ice particles and supercooled droplets, thereby favoring riming (Korolev, 2007; Korolev and Field, 2008; Chellini and Kneifel, 2024). High SLWP is therefore regarded as a physically favorable regime in which riming should occur more frequently.

Figure 5 presents a case of an LLMPC observed over the Southern Ocean on 12 January 2025. The cloud remains confined below about 2 km altitude throughout the scene (Fig. 5a). The collocated ECMWF temperature field places cloud-top temperatures (CTTs) near −10 °C and indicates a temperature inversion near cloud top. The inversion, also evident in the corresponding temperature profile (not shown), helps confine the cloud to a shallow layer. Even over such a limited vertical extent, ice particles attain sedimentation velocities exceeding 1.0 m s^{-1} along much of the transect (purple in Fig. 5b), values not observed in the deeper cloud shown in Fig. 3. Correspondingly, G_V exceeds the 0.4 m s^{-1} km^{-1} riming threshold there and frequently surpasses 0.6 m s^{-1} km^{-1} (Fig. 5c). Figure 5d shows the riming regions meeting the detection criteria (blue), which are concentrated between the SLW top and SLW base (filled and open circles, respectively). The SLW boundaries are derived independently of the Doppler measurements used for riming detection. In particular, the SLW base is inferred from the SLWP (teal dots in Fig. 5e), itself estimated from PIA (orange dots in Fig. 5e), assuming an adiabatic liquid layer. No SLW base is shown where a reliable SLWP estimate cannot be obtained. The most continuous and deepest riming signatures are detected

https://doi.org/10.5194/egusphere-2026-6312
Preprint. Discussion started: 23 October 2026
© Author(s) 2026. CC BY 4.0 License.

where the inferred SLWP exceeds approximately 200 g m^{-2}, consistent with the expectation that riming occurs more frequently in environments with abundant SLW.

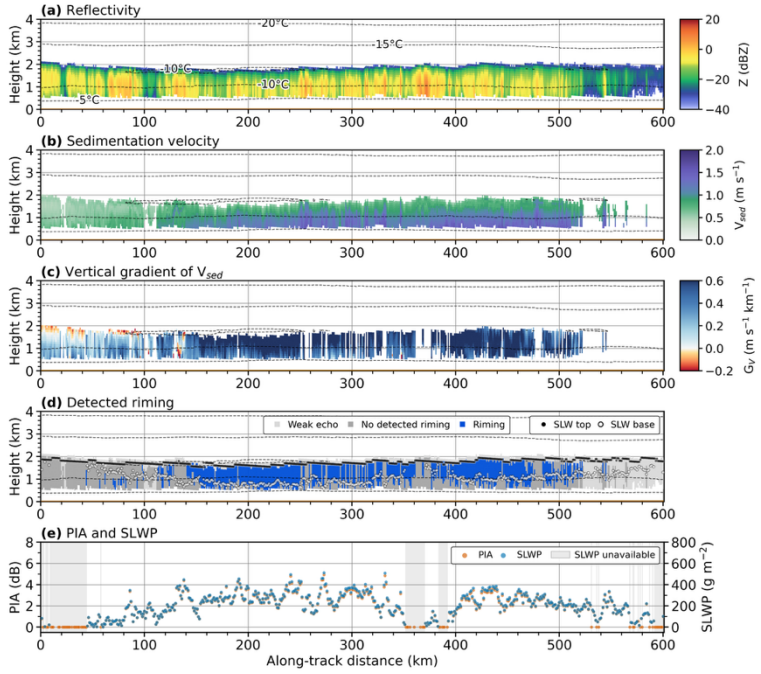


Figure 5: Example of a low-level mixed-phase cloud (LLMPC) observed by EarthCARE over the Southern Ocean on 12 January 2025 (Orbit/Frame ID: 03550H). Panels (a)–(d) show reflectivity, sedimentation velocity, the vertical gradient of sedimentation velocity, and the detected riming (blue areas), respectively. Filled and open circles in panel (d) indicate the ATLID-detected SLW top and the estimated SLW base. Panel (e) shows path-integrated attenuation (PIA; orange dots) and the corresponding supercooled liquid water path (SLWP; teal dots) where available. In this case, areas without an SLWP estimate (gray shading) are mostly found where PIA is 0 dB.

The SLW layer, however, is not uniformly occupied by riming signatures. Between roughly 50 and 100 km along the transect, little or no riming is detected within the SLW layer despite reflectivities comparable to those in adjacent regions where riming is detected (Fig. 5a). Sedimentation velocities remain close to 0.5 m s^{-1} there (Fig. 5b), pointing instead to relatively small ice particles dominating the estimated SLW layer. Riming may therefore be absent, or too limited to produce a measurable increase in fall speed. It is also possible that the estimated SLW layer does not fully represent the actual vertical distribution of liquid water in this part of the cloud. If the liquid water were present in multiple layers, the assumption used to derive SLWP and the SLW base would no longer be valid, and the primary SLW layer could instead reside farther below. Indeed, a few riming signatures are detected below the estimated SLW base. Even if so, riming signatures are only sporadically detected. Compared with the adjacent riming regions, SLWP is generally lower, remaining below about 200 g m^{-2} and often below 100 g m^{-2}. Such conditions may simply not favor riming that is detectable by the present method.

https://doi.org/10.5194/egusphere-2026-6312
Preprint. Discussion started: 23 October 2026
© Author(s) 2026. CC BY 4.0 License.

A different example is found beyond about 520 km along the transect. Except for an isolated cell near 545 km, reflectivities mostly fall below the −21 dBZ threshold required for reliable V_{SED} retrievals, leaving G_V unavailable. We therefore cannot determine whether riming occurs in this part of the cloud. Additional LLMPC examples are provided in Figs. S1–S5 in the Supplement.

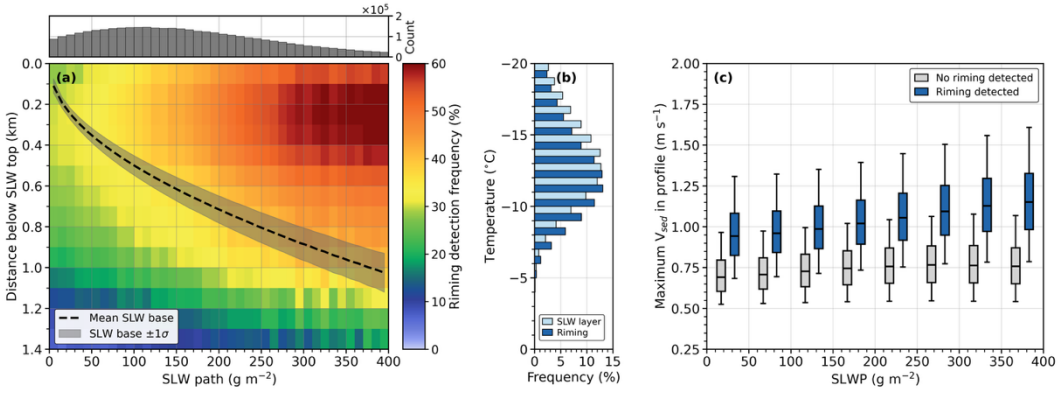


Figure 6: (a) Riming detection frequency for LLMPCs from one year of EarthCARE observations in 2025 as a function of distance below the SLW top and SLWP. Bin sizes are 100 m and 10 g m^{-2}, respectively. The black dashed line and gray shading indicate the estimated mean SLW base and its standard deviation. Bars above indicate the number of gates in each SLWP bin. (b) Temperature distributions of the SLW layer (between the SLW top and base; light blue) and detected riming (blue), using 1 °C bins. (c) Distributions of the maximum V_{SED} in profiles with and without riming detection (blue and gray, respectively) as a function of SLWP. Boxplots are presented in 50 g m^{-2} SLWP bins and follow the format of Fig. 3f.

Figure 6 extends the analysis to the full year of EarthCARE observations for LLMPCs. In Fig. 6a, riming detection frequency is summarized as a function of SLWP and distance below the SLW top. The estimated mean SLW base (dashed black line) and its ±1σ variability (gray shading) are also shown. Attenuation of about 1 dB, corresponding to roughly 125 g m^{-2} of SLWP near −15 °C, or less is comparable in magnitude to the typical PIA retrieval uncertainty, so low SLWP conditions may be more susceptible to being missed. If the assumptions used to estimate the SLW base were always valid, riming would be expected only within the estimated SLW layer. Instead, the detection frequency does not approach zero below the estimated SLW base. As seen in Fig. 5, this may reflect cases in which the liquid layer is more vertically complex than assumed, for example when multiple liquid layers are present. Vertical smoothing in the detection may also extend the riming signal below the estimated SLW base. A clear dependence on SLWP nevertheless emerges. Once SLWP exceeds about 200 g m^{-2}, the detection frequency often exceeds 50% within the estimated SLW layer. Given that fewer than about 0.5% of the null reference gates satisfy the same criteria (Sect. 3.2), their frequent occurrence under mixed-phase conditions with abundant SLW supports their interpretation as signatures of riming.

Likewise, the temperature distribution of detected riming broadly follows that of the SLW layer (Fig. 6b; riming in blue and the SLW layer in light blue). The slight warmward shift of the riming distribution, about 1–2 °C, could partly reflect riming

https://doi.org/10.5194/egusphere-2026-6312
Preprint. Discussion started: 23 October 2026
© Author(s) 2026. CC BY 4.0 License.

beginning farther below the SLW top, but it is also influenced by the detection methodology. The vertical window used to estimate G_V (i.e., 1 km) broadens the detected layer, while the upper part is preferentially missed because ice particles near the SLW top often fall below the 0.5 m s^{-1} threshold for riming detection. The relatively limited extension toward warmer temperature is also an expected consequence of the sampling, since the LLMPC subset consists of shallow clouds with subfreezing temperatures at all levels. In other words, sampling is biased toward SLW layers near cloud top, where temperatures remain relatively low. Even acknowledging that WBF-driven depositional growth, followed by aggregation, may occur in these mixed-phase clouds, the pronounced increase in V_{SED} over the temperature range shown in Fig. 6b is difficult to reconcile with those processes alone. As shown in Figs. 2 and 4, ice growth other than riming between about −18 and −12 °C generally limits increases in V_{SED} and often even reduces it. Accordingly, among the known ice growth mechanisms, riming provides the most straightforward explanation of these observations.

Figure 6c further compares the maximum V_{SED} as a function of SLWP between profiles with detected riming (blue) and those without (gray). The former consistently reach larger maximum V_{SED} (median differences of at least 0.25 m s^{-1}), as expected from detection criteria requiring rapid increases in V_{SED}. The more notable difference lies in the SLWP dependence. Maximum V_{SED} continues to increase with SLWP when riming is detected, whereas only a weak increase is found otherwise before leveling off. This behavior resembles the main findings of Chellini and Kneifel (2024). They showed that, in LLMPCs, particle fall speeds respond strongly to increasing liquid water when turbulent mixing enhances riming, whereas the response remains much weaker under weakly turbulent conditions. Although the present EarthCARE observations do not yet permit an assessment of turbulence (e.g., the eddy dissipation rate), profiles without riming may preferentially represent clouds with weaker turbulent mixing. If so, this would explain part of the riming detection frequencies remaining below 100% in Fig. 6a despite abundant SLW. Together, these findings provide consistent physical support for interpreting the detected signatures as riming.

4 Evaluation of Riming Detection with Collocated Aircraft Observations

A unique aspect of the EarthCARE mission is the extensive use of coordinated underflight campaigns, which provide complementary observations unavailable from the satellite alone. This study focuses on Flight 7 of the ECALOT campaign, during which the NRC Convair-580 aircraft sampled a mixed-phase cloud system northwest of Ottawa, over western Quebec. The flight consisted of three horizontal legs along and around the satellite ground track. The second leg was flown to coincide with the EarthCARE CPR overpass, which occurred near 19:30:42 UTC, and is used here for comparison with the EarthCARE observations.

Figure 7 presents observations from the NAW radar (Fig. 7a, c), the in situ instruments (Fig. 7e), and the EarthCARE CPR (Fig. 7b, d) during the direct underpass. The EarthCARE observations are aligned with the aircraft transect by mapping each satellite profile to the nearest position along the continuous Convair-580 flight track. The Convair-580 traversed the transect at an altitude of approximately 1.7 km (horizontal solid line) over about 28 min, with the EarthCARE overpass occurring near

https://doi.org/10.5194/egusphere-2026-6312
Preprint. Discussion started: 23 October 2026
© Author(s) 2026. CC BY 4.0 License.

the midpoint of the transect (vertical dashed line), whereas the satellite covered the corresponding distance in about 20 s. The maximum temporal separation is therefore about 14 min near the ends of the transect, decreasing toward the overpass location, where the observations are nearly coincident in time. Both radars depict a similar cloud structure in reflectivity (Fig. 7a, b), as expected for observations of the same cloud scene at W-band. The remaining differences likely reflect differences in sensitivity, spatial resolution, viewing geometry, and blind zones of the two radar systems, as well as cloud evolution. In particular, the finer spatial resolution of the airborne radar resolves smaller-scale features, such as ice-generating cells near cloud top. We do not attempt a quantitative interpretation of the airborne Doppler velocity (Fig. 7c) because the effects of aircraft motion have not yet been corrected.

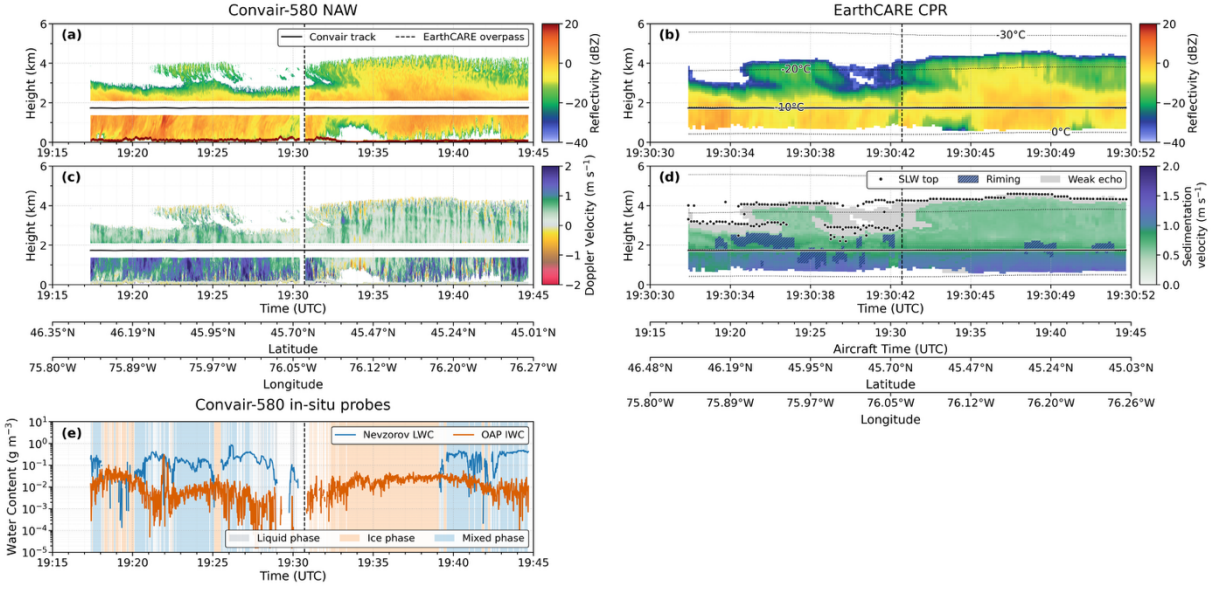


Figure 7: Collocated EarthCARE (Orbit/Frame ID: 04681D) and NRC Convair-580 observations acquired during ECALOT Flight 7 on 25 March 2025. Panels (a) and (c) show reflectivity and Doppler velocity from the NRC NAW, and panels (b) and (d) show EarthCARE CPR reflectivity and sedimentation velocity. EarthCARE observations are mapped to the nearest position along the Convair-580 flight track. The horizontal solid and vertical dashed lines denote the flight altitude and the point of satellite–aircraft coincidence, respectively. In panel (d), detected riming is shown as blue hatched areas. Black dots indicate the ATLID-detected SLW top. Panel (e) shows liquid water content (LWC; blue line) from the Nevzorov probe and ice water content (IWC; orange line) from the optical array probes (OAP). Background shading indicates cloud phase based on LWC and IWC thresholds of 0.01 and 0.001 g m^{-3}, respectively.

The primary value of the aircraft observations lies in the in situ microphysical measurements. Figure 7e shows the LWC (blue line) and IWC (orange line) measured at flight level. For reference, cloud phase was identified using LWC and IWC thresholds of 0.01 and 0.001 g m^{-3}, respectively. The lower IWC threshold was adopted to avoid missing small amounts of ice. At flight level, conditions are mainly mixed-phase (blue shading) before the EarthCARE overpass, although local ice-phase regions (orange shading) are also present. After the overpass, ice phase occupies about two-thirds of the remaining transect before

https://doi.org/10.5194/egusphere-2026-6312
Preprint. Discussion started: 23 October 2026
© Author(s) 2026. CC BY 4.0 License.

mixed-phase returns near the end. Meanwhile, ATLID detects SLW near cloud top in almost every profile (black dots in Fig. 7d).

The CPI onboard the Convair-580 provides direct images of individual hydrometeors, allowing ice particle habits to be examined directly. In mixed-phase regions, however, the recorded images may be biased toward supercooled droplets. This reflects the CPI sampling strategy. Higher particle concentrations increase the likelihood of CPI triggering, so the recorded images preferentially sample particle-rich volumes (Lawson et al., 2001). As a result, where mixed phase is identified, the CPI images consist almost entirely of supercooled droplets, and ice particles are captured only occasionally where droplet concentrations are relatively low.

Figure 8 assembles all CPI images capturing ice particles within the region of interest, excluding supercooled droplets, into 1-min time bins. The image selection was performed automatically, and particles smaller than 100 μm were excluded because they were predominantly supercooled droplets. As expected, ice particles are only sparsely observed in the mixed-phase region but are relatively abundant in the ice-phase region. Before the EarthCARE overpass (approximately 19:31 UTC), rimed particles appear frequently, even though only a limited number of ice particles are detected. For example, ice particles observed around 19:17–19:18 and 19:21–19:22 UTC are small but appear heavily rimed. The particles no longer retain a recognizable crystal shape but instead appear lumpy and nearly rounded. Around 19:19–19:20 UTC, the particles are relatively larger and retain their branched shapes, but rime accretions are still visible near branch tips and edges. The presence of rimed particles in regions classified as ice phase at flight level suggests that they acquired rime higher in the cloud.

https://doi.org/10.5194/egusphere-2026-6312
Preprint. Discussion started: 23 October 2026
© Author(s) 2026. CC BY 4.0 License.

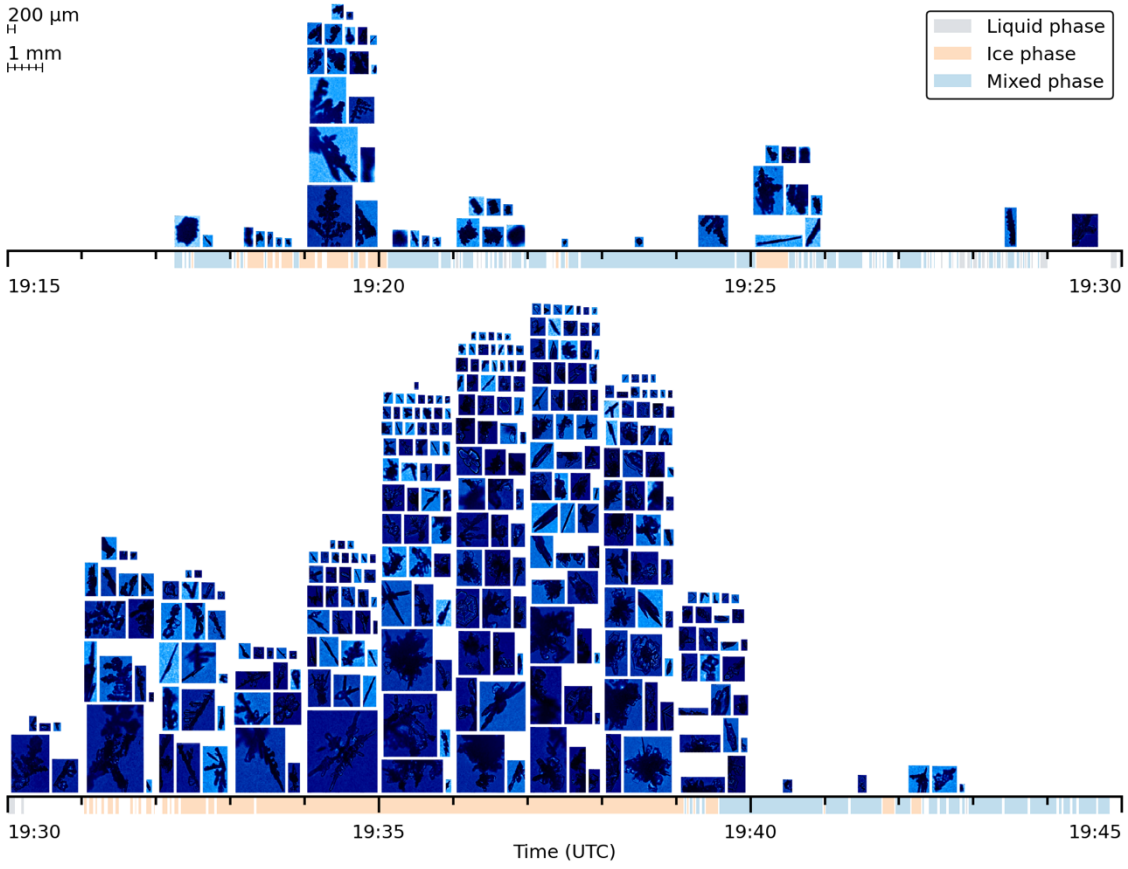


Figure 8: Cloud particle imager (CPI) images of ice particles from the flight transect shown in Fig. 7. Images observed within each 1 min interval are shown together, where larger images are generally placed toward the bottom. The colored strip beneath the time axis indicates the cloud phase from Fig. 7e.

560

The riming detections in Fig. 7d (blue hatched regions) are broadly consistent with the CPI observations, showing frequent riming before the overpass. They do not, however, account for every particle that appears rimed in the CPI images. Between about 19:17 and 19:19 UTC, for example, the CPI recorded a few particles with visible signs of riming, but no corresponding signature is detected at or above that location. This could reflect riming confined to spatial scales too small to be captured by
565 the riming detection, or riming that had not yet progressed far enough to produce the velocity increase used to identify it. The possibility of horizontal advection of sedimenting ice particles also cannot be entirely ruled out. The altitude at which riming is first detected also varies. This may depend on variations in the vertical distribution of the dominant SLW layer, or differences in the size and habit of the ice crystals when they first encounter it. Yet the present observations do not allow these possibilities to be distinguished.

570 The situation changes in the extensive ice-phase region between about 19:31 and 19:39 UTC. Aside from a brief period of slightly rimed crystals during the first minute, the CPI images show little evidence of riming (Fig. 8). Plates, dendrites, needles,

https://doi.org/10.5194/egusphere-2026-6312
Preprint. Discussion started: 23 October 2026
© Author(s) 2026. CC BY 4.0 License.

and their aggregates are common throughout the ice-phase region. Some particles are difficult to classify confidently, particularly when the images are slightly out of focus. Most nevertheless retain discernible remnants of the original crystal habit along the particle edges (e.g., the lower right image at 19:38–19:39 UTC), supporting the interpretation that they are aggregates rather than rimed particles. This suggests that the cloud provided little opportunity for riming, not only at the flight level but also higher in the cloud where the ice particles formed and grew. This is reflected in the riming detection, where little riming is detected through most of the cloud above the flight level (Fig. 7d), except for a small area near 19:39–19:40 UTC. This feature is contiguous with the adjacent mixed-phase riming region and may reflect the spatial smoothing applied in the V_{SED} retrieval. Even so, the overall agreement between the CPI observations and the riming detection suggests that ice particles growing without riming in this case were generally not associated with the sedimentation velocity acceleration defined as a riming signature (i.e., ≥ 0.4 m s^{-1} km^{-1}).

5 Global Distribution of Riming Detection Frequency

EarthCARE's orbital coverage allows riming to be examined across most of the globe. Figure 9 shows the distribution of riming detection frequency in stratiform clouds observed during 2025. We focus on temperatures warmer than −20 °C, where riming is most likely. Riming detection frequency (Fig. 9b) is defined as the ratio of detected riming gates to the total number of target gates within each grid cell (Fig. 9a). Both quantities are calculated on a 5° × 5° grid. Given the CPR's nadir-only sampling and infrequent revisits, the observations accumulated over one year may be insufficient for precise estimates of riming detection frequency in some grid cells. For the low detection frequencies encountered here, the absolute precision caused by finite sampling becomes larger as the detection frequency itself gets larger. Grid cells with insufficient precision, defined here by a nominal 95% Wilson confidence interval half-width greater than 0.25 percentage points, are marked by hatching. For example, this criterion requires approximately 12,100 target gates at a riming detection frequency of 2% and 55,300 at 10%. However, neighboring gates are correlated, so these intervals may underestimate the actual sampling uncertainty. The riming detection frequency field was rendered at 2.5° spacing with Gaussian smoothing to better reveal the broader spatial patterns.

Earlier satellite climatologies document frequent deep convection and mesoscale convective systems across the tropics and subtropics, especially over tropical Africa, Amazonia, the western Pacific warm pool, and the oceanic intertropical convergence zones (Houze et al., 2015; Feng et al., 2021). Their strong convective updrafts are expected to favor efficient riming and graupel growth. The map in Fig. 9b, however, shows low riming detection frequencies across these regions, as it represents riming only within the stratiform clouds that remain after convective screening. Strongly forced orographic clouds may also be underrepresented, as their V_{SED} error or variability frequently exceeds the screening thresholds.

Riming detection frequency shows pronounced regional patterns. Prominent regions of high riming detection frequency include the Southern Ocean, the northwest Pacific, the northwest Atlantic, the Nordic Seas, and the Sichuan Basin of southwestern China, with values often exceeding 10%. The oceanic pattern broadly follows the major midlatitude storm tracks,

https://doi.org/10.5194/egusphere-2026-6312
Preprint. Discussion started: 23 October 2026
© Author(s) 2026. CC BY 4.0 License.

where frontal cloud systems and postfrontal shallow mixed-phase clouds are common and may favor riming (Korolev et al., 2017). The Nordic Seas also experience frequent cold-air outbreaks during winter and spring, producing extensive shallow convective mixed-phase clouds where riming is expected to occur readily (Geerts et al., 2022; Kim et al., 2026). The Sichuan Basin is particularly noteworthy as one of the most pronounced continental maxima in riming detection frequency. Previous studies indicate that the Tibetan Plateau diverts the low-level westerlies around its northern and southern flanks. Parts of these flows subsequently converge over the Sichuan Basin, lifting warm and moist air into a layer capped by a midlevel temperature inversion (for a detailed discussion of these processes, see Li and Gu, 2006; Zhang et al., 2013). This combination supports persistent midlevel stratiform clouds that can sustain SLW, particularly during the cold season, and may help explain the enhanced riming observed there. One illustrative case from each of these regions is provided in Figs. S6–S10 in the Supplement.

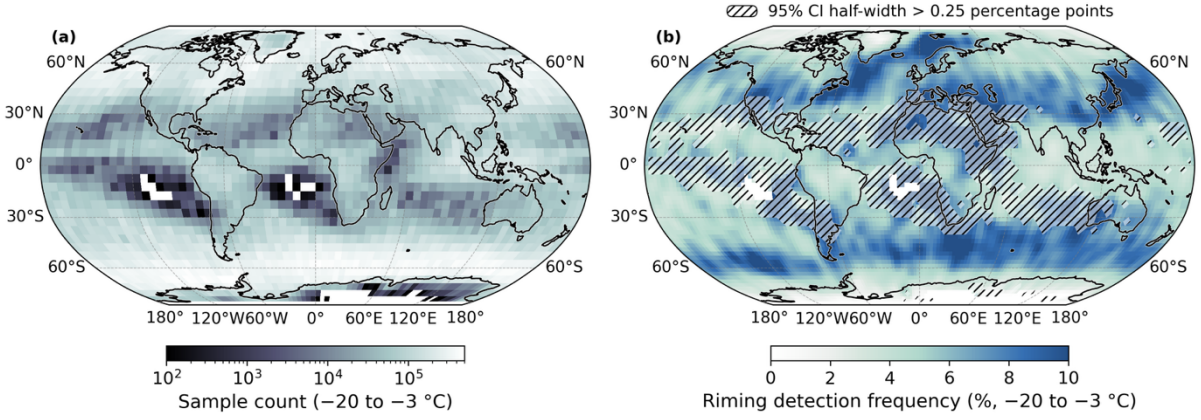


Figure 9: Global distributions of (a) sample count for the targeted echoes and (b) riming detection frequency in stratiform clouds between −20 and −3 °C during 2025. Both quantities are calculated on a 5° × 5° grid. For visualization, the riming detection frequency in panel (b) is rendered at 2.5° spacing with light smoothing. Hatching marks grid cells where the nominal 95% Wilson confidence interval (CI) half-width exceeds 0.25 percentage points (i.e., less precise estimates).

This regional pattern is broadly consistent with the global distribution of supercooled water cloud detections reported by Hu et al. (2010) and Battaglia and Delanoë (2013) using the Cloud-Aerosol Lidar with Orthogonal Polarization (CALIOP). However, detecting SLW does not by itself imply riming. Efficient droplet accretion onto ice requires a sufficient reservoir of liquid water, likely sustained by dynamical processes such as ascent or turbulent mixing. Moreover, lidar can detect only the top of the first liquid layer encountered from above, and even then only if its signal has not already been fully extinguished by overlying clouds. The present method instead detects the imprint of riming directly in sedimentation velocity, including where it occurs within cloud layers that lidar cannot penetrate. This study therefore presents the first near-global satellite view of riming in stratiform clouds. As the EarthCARE record grows, these observations are expected to reveal more clearly how riming depends on cloud regime and meteorological environment across regions and seasons, and to provide a valuable benchmark for evaluating its representation in weather and climate models.

https://doi.org/10.5194/egusphere-2026-6312
Preprint. Discussion started: 23 October 2026
© Author(s) 2026. CC BY 4.0 License.

630

6 Summary and Discussion

This study developed and evaluated a method for detecting riming in stratiform clouds using the downward vertical gradient of hydrometeor sedimentation velocity from the EarthCARE CPR Corrected Doppler Measurements (C-CD) product. The method isolates the sharp increase in V_{SED} associated with accumulating rime mass from the more gradual rise produced by vapor deposition and aggregation. The detection criterion was set from the upper tail of the G_V distribution in ice/snow-only regions, where the ATLID signal remained unextinguished and no SLW was detected, and required $G_V \geq 0.4$ m s^{-1} km^{-1} at three or more consecutive vertical gates. Once convective profiles, melting layer contamination, uncertain V_{SED} retrievals (error ≥ 0.25 m s^{-1} or variability ≥ 0.6 m s^{-1}), very weak sedimentation ($V_{SED} < 0.5$ m s^{-1}), and sublimation ($G_Z < 0$ dBZ km^{-1}) were removed, fewer than 0.5% of the ice/snow-only gates, treated as the non-riming reference population, met this criterion over the temperature range from −40 to −3 °C (Fig. 4). This low occurrence indicates that such sharp, vertically coherent increases in V_{SED} are rarely observed where riming is not expected.

In the absence of ground truth that resolves riming throughout the cloud column, conventional measures of detection accuracy cannot be established. We therefore evaluated the detected signatures in low-level mixed-phase clouds (LLMPCs) over ocean, where EarthCARE observations offer practical constraints on the amount and vertical extent of SLW. The detected riming regions were concentrated within the estimated SLW layer, and once SLWP exceeded about 200 g m^{-2}, the riming detection frequency often surpassed 50% within that layer (Fig. 6a).

These results should nevertheless be interpreted within the limitations of the SLW estimates. The inferred layer assumes that liquid water occupies a single layer concentrated near cloud top, an approximation that may not hold when SLW is distributed across separate levels or when the principal liquid layer lies farther below. Weak attenuation presents an additional limitation because a PIA of about 1 dB (roughly 125 g m^{-2} of SLWP near −15 °C) can be comparable to its retrieval uncertainty (Sasikumar et al., 2026), causing low SLWP conditions to be undersampled in the evaluation. SLW can be better estimated as attenuation strengthens, but riming is not invariably detected even when SLW is abundant. One possibility is that some clouds contain too little ice, or particles too small, to collect droplets efficiently. Riming may then be absent or too weak to meet the present detection criterion. Weak turbulent mixing may also limit encounters between ice particles and supercooled droplets. The available observations cannot determine whether the absence of detection reflects genuinely limited riming or riming that occurred without producing a sufficiently strong increase in V_{SED}.

The coordinated ECALOT underflight provided valuable case-level evidence (Figs. 7 and 8). Despite the sparse CPI sampling of ice particles in mixed-phase regions, rimed particles were frequently observed within or below the regions identified as riming by the present method. In the ice-phase region, where the CPI recorded predominantly unrimed single crystals (e.g., plates, dendrites, and needles) and aggregates, little riming was detected through most of the cloud at or above flight level.

https://doi.org/10.5194/egusphere-2026-6312
Preprint. Discussion started: 23 October 2026
© Author(s) 2026. CC BY 4.0 License.

Although limited to a single case, this clear contrast supports the central premise that vapor deposition and aggregation generally do not produce the sharp increase in V_{SED} used here to identify riming.

An important aspect of the method is that it is designed to detect where riming is occurring, not where rimed particles are present. The signal is expected to arise where sedimenting ice particles acquire rime mass and V_{SED} increases rapidly. After leaving the liquid-containing layer, particles may retain the rime acquired above and continue into regions where sublimation occurs. They are no longer detected once the sharp increase in V_{SED} ceases. In other words, the method identifies regions where riming is actively modifying the ice particles, even though rimed particles may persist farther below.

The distinction between riming and the presence of rimed particles is consequential because they answer different observational questions. Identifying active riming locates where SLW is being transferred to ice and provides an observational counterpart to modeled riming tendencies, particularly in property-evolving schemes such as the Predicted Particle Properties (P3; Morrison and Milbrandt, 2015) and the Ice-Spheroids Habit Model with Aspect-Ratio Evolution (ISHMAEL; Jensen et al., 2017). The method also provides an indirect view of SLW that is sufficiently abundant to produce detectable riming. It can reveal liquid-bearing layers embedded within optically thick or multilayer clouds where ATLID is extinguished, complementing lidar-based maps of SLW. By contrast, applications concerned with the subsequent mass, density, or scattering properties of rimed ice require identification of rimed particles themselves. For example, radar retrievals of IWC and particle characteristic size may benefit from identifying rimed particles after they leave the layer in which the rime was acquired. Extending the detection downward to identify rimed particles would require assuming that particles carrying the inherited riming signature continue to dominate the radar return as they sediment. However, horizontal advection, sublimation, and secondary ice production can alter that composition with height. Determining how far a rimed particle classification can be carried below the detected riming layer therefore requires separate investigation.

Ultimately, this study establishes a way to constrain riming from space and provides the first near-global climatological view of riming detection frequency in stratiform clouds (Fig. 9). The scientific value of this climatology is expected to grow with continued sampling by providing a more robust basis for examining broadly recurring thermodynamic and microphysical conditions that favor riming and documenting its variability across regions and seasons. These observations also offer a new observational constraint for evaluating representations of riming in weather and climate models and for improving simulations of cloud evolution, precipitation formation, and cloud radiative effects.

https://doi.org/10.5194/egusphere-2026-6312
Preprint. Discussion started: 23 October 2026
© Author(s) 2026. CC BY 4.0 License.

Appendix A: Air Density Correction for Sedimentation Velocity

Hydrometeor fall speeds are intrinsically dependent on the ambient air density (ρ), as aerodynamic drag experienced by a falling particle varies with air density. To enable a physically consistent comparison of particle fall speeds across varying altitudes and environmental conditions, all CPR-retrieved sedimentation velocities (V_{SED}) in this study are normalized to a reference state.

Following the formulation of Foote and du Toit (1969), the observed velocity (V_h) at a given altitude h is corrected to a reference velocity (V_{ref}) at mean sea level (MSL) as follows:

$$V_{ref} = V_h \cdot \left(\frac{\rho_h}{\rho_{ref}}\right)^{\kappa}, \quad \text{(A1)}$$

where ρ_h is the air density at the level of observation and ρ_{ref} is the reference air density at MSL. The exponent κ is an empirical air-density correction factor that describes how fall speed scales with air density; consistent with previous radar studies (e.g., Foote and du Toit, 1969; Atlas et al., 1973), we utilize a value of $\kappa = 0.4$. By applying the ideal gas law, this relationship can be expressed in terms of pressure (P) and temperature (T):

$$V_{ref} = V_h \cdot \left(\frac{P_h}{T_h} \cdot \frac{T_{ref}}{P_{ref}}\right)^{0.4}. \quad \text{(A2)}$$

In this study, we adopt the reference values P_{ref} = 101,300 Pa and T_{ref} = 293 K. The pressure and temperature fields required for this correction are obtained from the ECMWF meteorological fields (X-MET). This normalization effectively mitigates the impact of air density variations, ensuring that the corrected V_{SED} primarily reflects the microphysical characteristics of the hydrometeors.

Appendix B: Gate-to-Gate Autocorrelation and Regression Window Selection

To obtain physically representative vertical gradients of sedimentation velocity (V_{SED}), the regression window must be carefully optimized. It must be sufficiently long to reduce the influence of gate-to-gate autocorrelation, yet short enough to avoid excessive smoothing. We therefore quantified the autocorrelation of V_{SED} and used it to guide the choice of the suitable regression window length based on the effective sample size.

This analysis was performed using one year of EarthCARE CPR observations during 2025. For each cloud profile, we first identified the longest continuous vertical segment of V_{SED} (minimum 20 gates) within regions where temperatures were below 0 °C. Within each segment, we removed the overall vertical trend by fitting a linear function of V_{SED} with height and computing the residuals. The autocorrelation function (ACF) was then evaluated from these residuals, such that the resulting correlation

https://doi.org/10.5194/egusphere-2026-6312
Preprint. Discussion started: 23 October 2026
© Author(s) 2026. CC BY 4.0 License.

structure reflects gate-to-gate dependence beyond the large-scale vertical variation of V_{SED}. The lag-k autocorrelation was computed following Wilks (2011):

$$ACF(k) \approx \frac{\sum_{t=1}^{n-k}(x_t-\bar{x})(x_{t+k}-\bar{x})}{\sum_{t=1}^{n}(x_t-\bar{x})^2}, \quad \text{(B1)}$$

where x_t denotes the V_{SED} residual at gate t, $\bar{x}$ is the mean residual within the segment, n is the segment length, and k represents the lag in units of vertical gates (100 m per gate).

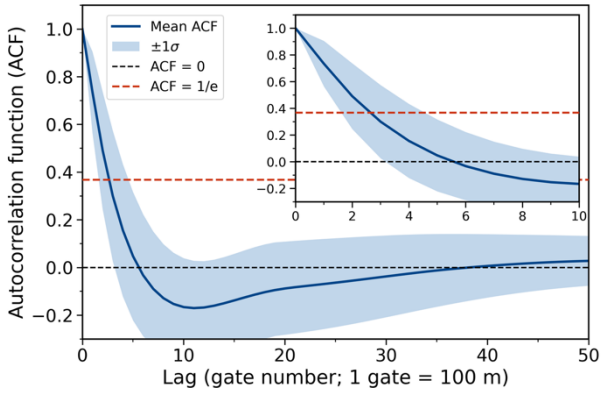


Figure B1: Autocorrelation function (ACF) of V_{SED} residuals calculated from one year of EarthCARE CPR data. The solid blue line indicates the mean ACF, while the shaded area represents the ±1σ variability. The dashed orange line denotes the 1/e decorrelation level. The inset provides a detailed view of the short-range correlation structure for lags 0 to 10.

The ACF, shown in Fig. B1, reveals substantial dependence between adjacent gates, with a mean lag-1 value of approximately 0.73. At a lag of two gates, the mean ACF decreases to about 0.49, and further decreases to about 0.30 at a lag of three gates, falling below the 1/e level. This indicates that the e-folding decorrelation length corresponds to approximately three gates. The mean ACF approaches zero between lags 5 and 6, indicating that most vertical dependence is confined to a spatial separation of about 500 m, consistent with the 500-m vertical pulse length of the CPR. Beyond this scale, the ACF remains near zero and does not return to the e-folding threshold.

Since adjacent gates are not independent, the nominal number of samples within a regression window overstates the amount of independent information available for estimating a vertical gradient. We therefore quantified the effective sample size (n_{eff}) following Wilks (2011):

$$n_{eff} = \frac{n}{1+2\sum_{k=1}^{n-1}(1-\frac{k}{n})\cdot\overline{ACF}(k)}. \quad \text{(B2)}$$

https://doi.org/10.5194/egusphere-2026-6312
Preprint. Discussion started: 23 October 2026
© Author(s) 2026. CC BY 4.0 License.

where n is the nominal number of gates in the regression window, and $\overline{ACF}(k)$ is the mean autocorrelation at lag k shown in Fig. B1. The relationship between nominal and effective sample size is shown in Fig. B2.

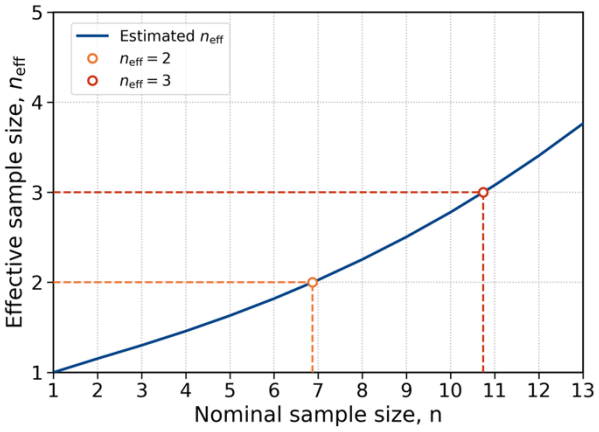


Figure B2: Effective sample size (n_{eff}) as a function of nominal regression window length (n), estimated from the mean ACF shown in Fig. B1 following Eq. (B2).

For a linear regression with fitted slope and intercept, at least three independent samples are required to retain one residual degree of freedom (DOF). Based on Fig. B2, this condition is first satisfied at $n = 11$. We therefore adopt 11 consecutive valid gates as the suitable window length for vertical gradient estimation in this study. On the CPR vertical resolution, this corresponds to a center-to-center distance of about 1 km.

In practice, an 11-gate window cannot always be maintained near cloud boundaries or other vertically limited regions of the profile. To preserve data coverage in such cases, the window is allowed to decrease gradually from 11 gates to a minimum of seven gates. This minimum was chosen because smaller windows would reduce the effective sample size to below two, thereby failing to provide the minimum DOF ($n_{eff} - 2 > 0$) required for a linear regression.

Appendix C: Riming Detections in Ice/Snow-Only Gates between −10 and −3 °C

Here we examine more closely the riming detections that remain in the ice/snow-only gates between −10 and −3 °C, where their occurrence is highest (Sect. 3.2). Figure C1 summarizes these detections in terms of their spatial extent, cloud top temperature, and proximity to ATLID-detected SLW. For Fig. C1a, we define each detected area as a contiguous group of pixels sharing an edge that meet the final riming criterion, where a single pixel corresponds to approximately 0.1 km^2. Their size distribution in the ice/snow-only gates (solid line) is shifted markedly toward smaller areas compared with riming detections in the targeted echoes between −10 and −3 °C (dotted line), reflecting their characteristically small and isolated

https://doi.org/10.5194/egusphere-2026-6312
Preprint. Discussion started: 23 October 2026
© Author(s) 2026. CC BY 4.0 License.

extent. As noted in Sect. 3.2, gates meeting the riming criterion account for about 2% of the ice/snow-only subset in this temperature range. Among these detections, approximately 35% occupy the minimum possible area of 0.3 km^2 imposed by the requirement for three vertically consecutive gates. A second clear characteristic is their preference for clouds with relatively warm tops (Fig. C1b). For comparison, reference profiles are drawn from the same temperature interval, requiring at least three vertically consecutive ice/snow-only gates but no riming detection. Reference profiles are randomly sampled 1000 times, and the same number of profiles as in the detected group is selected each time. Figure C1b shows the median cumulative distribution of cloud top temperature. The 5th to 95th percentile range is nearly indistinguishable from the median (not shown here). The detected cases are strongly shifted toward warmer cloud tops, with approximately 75% occurring in clouds warmer than −20 °C compared with about 30% of the reference profiles. The detections are also preferentially located near profiles containing ATLID-detected SLW (Fig. C1c). Approximately half of the detected cases lie within two profiles of the nearest SLW detection. Overall, the riming detections in the −10 to −3 °C ice/snow-only gates tend to be small and occur preferentially in clouds with relatively warm tops and nearby SLW.

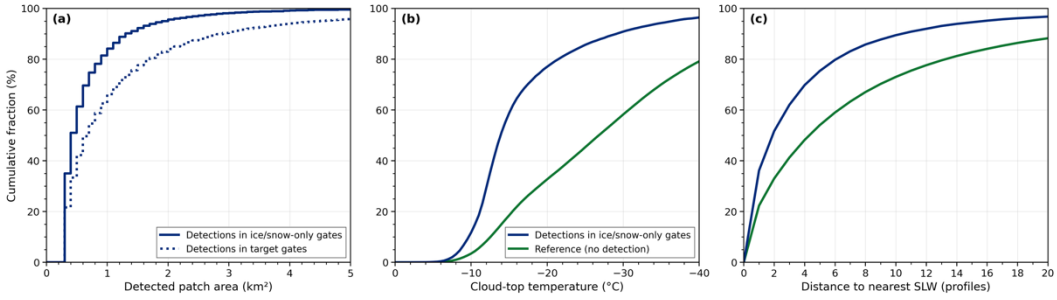


Figure C1: Cumulative distributions for detections in ice/snow-only gates between −10 and −3 °C. Panel (a) shows the area of connected detection patches in the ice/snow-only subset (solid line) and in the target gates (dotted line). Panels (b) and (c) show cloud top temperature and proximity to ATLID-detected SLW for profiles containing detections (blue) and reference profiles with no detection (green). The median reference distribution is shown.

Data availability

The EarthCARE Level-2 products (C-FMR, C-CD, C-TC, and AC-TC) used in this study are publicly available through the ESA Multi-Mission Algorithm and Analysis Platform (MAAP) Explorer (https://explorer.maap.eo.esa.int; last access: 9 October 2026) (European Space Agency, 2025, 2026a, 2026b, 2026c). The ECALOT airborne radar and in situ microphysical data used in this study are available through the ESA Validation Data Centre (EVDC; https://evdc.esa.int/search; last access: 9 October 2026). Registration is required to access and download the data.

Supplement link

The link to the supplement will be included by Copernicus, if applicable.

https://doi.org/10.5194/egusphere-2026-6312
Preprint. Discussion started: 23 October 2026
© Author(s) 2026. CC BY 4.0 License.

Author contributions

JK designed and performed the analysis, curated the data, prepared the visualizations, and wrote the original draft. PK supervised the study and contributed to the study design and methodology. BPT provided the EarthCARE data products and technical guidance on their use. AB provided scientific guidance on the interpretation of the EarthCARE observations and results. ZQ and CN provided expertise on the ECALOT observations and their interpretation. All authors contributed to the review and editing of the manuscript.

Competing interests

The authors declare that they have no conflict of interest.

Disclaimer

Copernicus Publications adds a standard disclaimer: "Copernicus Publications remains neutral with regard to jurisdictional claims made in the text, published maps, institutional affiliations, or any other geographical representation in this paper. While Copernicus Publications makes every effort to include appropriate place names, the final responsibility lies with the authors. Views expressed in the text are those of the authors and do not necessarily reflect the views of the publisher."

Please feel free to add disclaimer text at your choice, if applicable.

Special issue statement

This article is part of the special issue "Early results from EarthCARE (AMT/ACP/GMD inter-journal SI)." It is not associated with a conference.

Acknowledgements

The authors gratefully acknowledge the EarthCARE Data, Innovation and Science Cluster (DISC) team for their continued development and validation of the ESA EarthCARE data products used in this study and for valuable scientific and technical discussions. The authors also thank Alexei Korolev of Environment and Climate Change Canada (ECCC) for preparing and documenting the ECALOT in situ microphysical data, and the National Research Council Canada (NRC) science team (Paloma Borque, Keyvan Ranjbar, Natalia Bliankinshtein, Kenny Bala) for their contributions to the ECALOT airborne observations used in this study. The authors also thank the broader ECALOT team for the planning, flight operations, and field support that enabled the coordinated aircraft underflight of EarthCARE. OpenAI's ChatGPT was employed solely for language editing purposes, and all AI-assisted changes were reviewed and approved by the authors.

https://doi.org/10.5194/egusphere-2026-6312
Preprint. Discussion started: 23 October 2026
© Author(s) 2026. CC BY 4.0 License.

Financial support

This research has been primarily supported by the European Space Agency (ESA) through the Scientific Investigations of the Vertical Air MOtion and hydrometeors Sedimentation rates from EarthCARE CPR (VAMOS) project (contract no. 4000147845/25/I/AG).

Review statement

The review statement will be added by Copernicus Publications listing the handling editor as well as all contributing referees according to their status anonymous or identified.

References

Abel, S. J., Boutle, I. A., Waite, K., Fox, S., Brown, P. R. A., Cotton, R., Lloyd, G., Choularton, T. W., and Bower, K. N.: The role of precipitation in controlling the transition from stratocumulus to cumulus clouds in a Northern Hemisphere cold-air outbreak, J. Atmos. Sci., 74, 2293–2314, https://doi.org/10.1175/JAS-D-16-0362.1, 2017.

Atlas, D., Srivastava, R. C., and Sekhon, R. S.: Doppler radar characteristics of precipitation at vertical incidence, Rev. Geophys., 11, 1–35, https://doi.org/10.1029/RG011i001p00001, 1973.

Battaglia, A. and Delanoë, J.: Synergies and complementarities of CloudSat–CALIPSO snow observations, J. Geophys. Res.-Atmos., 118, 721–731, https://doi.org/10.1029/2012JD018092, 2013.

Bergeron, T.: On the physics of clouds and precipitation, in: Proceedings of the 5th Assembly of the UGGI, pp. 156–180, Lisbon, Portugal, 1935.

Bony, S., Stevens, B., Frierson, D. M. W., Jakob, C., Kageyama, M., Pincus, R., Shepherd, T. G., Sherwood, S. C., Siebesma, A. P., Sobel, A. H., Watanabe, M., and Webb, M. J.: Clouds, circulation and climate sensitivity, Nat. Geosci., 8, 261–268, https://doi.org/10.1038/ngeo2398, 2015.

Brown, P. R. A. and Francis, P. N.: Improved measurements of the ice water content in cirrus using a total-water probe, J. Atmos. Ocean. Technol., 12, 410–414, https://doi.org/10.1175/1520-0426(1995)012<0410:IMOTIW>2.0.CO;2, 1995.

Ceppi, P., Brient, F., Zelinka, M. D., and Hartmann, D. L.: Cloud feedback mechanisms and their representation in global climate models, WIREs Clim. Change, 8, e465, https://doi.org/10.1002/wcc.465, 2017.

Cesana, G., Waliser, D. E., Jiang, X., and Li, J.-L. F.: Multimodel evaluation of cloud phase transition using satellite and reanalysis data, J. Geophys. Res.-Atmos., 120, 7871–7892, https://doi.org/10.1002/2014JD022932, 2015.

Chellini, G. and Kneifel, S.: Turbulence as a key driver of ice aggregation and riming in Arctic low-level mixed-phase clouds, revealed by long-term cloud radar observations, Geophys. Res. Lett., 51, e2023GL106 599, https://doi.org/10.1029/2023GL106599, 2024.

https://doi.org/10.5194/egusphere-2026-6312
Preprint. Discussion started: 23 October 2026
© Author(s) 2026. CC BY 4.0 License.

DeLaFrance, A., McMurdie, L. A., Rowe, A. K., and Conrick, R.: Effects of riming on ice-phase precipitation growth and transport over an orographic barrier, J. Adv. Model. Earth Syst., 16, e2023MS003 778, https://doi.org/10.1029/2023MS003778, 2024a.

DeLaFrance, A., McMurdie, L. A., Rowe, A. K., and Heymsfield, A. J.: Simulated particle evolution within a winter storm: Contributions of riming to radar moments and precipitation fallout, Atmos. Chem. Phys., 24, 11 191–11 206, https://doi.org/10.5194/acp-24-11191-2024, 2024b.

Eisinger, M., Marnas, F., Wallace, K., Kubota, T., Tomiyama, N., Ohno, Y., Tanaka, T., Tomita, E., Wehr, T., and Bernaerts, D.: The EarthCARE mission: Science data processing chain overview, Atmos. Meas. Tech., 17, 839–862, https://doi.org/10.5194/amt-17-839-2024, 2024.

European Space Agency: EarthCARE ATLID CPR TC Level 2B, version BC, European Space Agency [data set], https://doi.org/10.57780/eca-0be60f4, 2025.

European Space Agency: EarthCARE CPR FMR Level 2A, version BD, European Space Agency [data set], https://doi.org/10.57780/esa-5dd2911, 2026a.

European Space Agency: EarthCARE CPR CD Level 2A, version BD, European Space Agency [data set], https://doi.org/10.57780/esa-af82d5d, 2026b.

European Space Agency: EarthCARE CPR TC Level 2A, version BD, European Space Agency [data set], https://doi.org/10.57780/esa-a4239d1, 2026c.

Feng, Z., Leung, L. R., Liu, N., Wang, J., Houze, R. A. Jr., Li, J., Hardin, J. C., Chen, D., and Guo, J.: A global high-resolution mesoscale convective system database using satellite-derived cloud tops, surface precipitation, and tracking, J. Geophys. Res.-Atmos., 126, e2020JD034 202, https://doi.org/10.1029/2020JD034202, 2021.

Feuillard, N., Toledo Bittner, F., Pfitzenmaier, L., Ribaud, J.-F., Delanoë, J., Haeffelin, M., and Dupont, J.-C.: Validation of EarthCARE CPR reflectivity using the ACTRIS cloud radar network, EGUsphere, https://doi.org/10.5194/egusphere-2026-925, 2026.

Findeisen, W.: Die kolloidmeteorologischen Vorgänge bei der Niederschlagsbildung, Meteorol. Z., 55, 121–133, 1938.

Foote, G. B. and du Toit, P. S.: Terminal velocity of raindrops aloft, J. Appl. Meteorol., 8, 249–253, https://doi.org/10.1175/1520-0450(1969)008<0249:TVORA>2.0.CO;2, 1969.

Forster, P., Storelvmo, T., Armour, K., Collins, W., Dufresne, J.-L., Frame, D., Lunt, D. J., Mauritsen, T., Palmer, M. D., Watanabe, M., Wild, M., and Zhang, H.: The Earth's energy budget, climate feedbacks, and climate sensitivity, in: Climate Change 2021: The Physical Science Basis. Contribution of Working Group I to the Sixth Assessment Report of the Intergovernmental Panel on Climate Change, edited by Masson-Delmotte, V., Zhai, P., Pirani, A., Connors, S. L., Péan, C., Berger, S., Caud, N., Chen, Y., Goldfarb, L., Gomis, M. I., Huang, M., Leitzell, K., Lonnoy, E., Matthews, J. B. R., Maycock, T. K., Waterfield, T., Yelekçi, O., Yu, R., and Zhou, B., pp. 923–1054, Cambridge University Press, Cambridge, United Kingdom and New York, NY, USA, https://doi.org/10.1017/9781009157896.009, 2021.

https://doi.org/10.5194/egusphere-2026-6312
Preprint. Discussion started: 23 October 2026
© Author(s) 2026. CC BY 4.0 License.

Frostenberg, H. C., Costa-Surós, M., Georgakaki, P., Proske, U., Sotiropoulou, G., May, E., Neubauer, D., Eriksson, P., Gonçalves Ageitos, M., Nenes, A., Pérez García-Pando, C., Seland, Ø., and Ickes, L.: Large discrepancies in dominant microphysical processes governing mixed-phase clouds across climate models, npj Clim. Atmos. Sci., 9, 75, https://doi.org/10.1038/s41612-026-01342-7, 2026.

Furtado, K. and Field, P.: The role of ice microphysics parametrizations in determining the prevalence of supercooled liquid water in high-resolution simulations of a Southern Ocean midlatitude cyclone, J. Atmos. Sci., 74, 2001–2021, https://doi.org/10.1175/JAS-D-16-0165.1, 2017.

Geerts, B., Giangrande, S. E., McFarquhar, G. M., Xue, L., Abel, S. J., Comstock, J. M., Crewell, S., DeMott, P. J., Ebell, K., Field, P., Hill, T. C. J., Johnson, K. L., Juliano, T. W., Kollias, P., Lackner, C. P., Luke, E. P., Matthews, A., Neggers, R. A. J., Ovchinnikov, M., Powers, H., Shupe, M. D., Spangenberg, D., Sullivan, S. C., Tjernström, M., and Wu, P.: The COMBLE Campaign: A study of marine boundary layer clouds in Arctic cold-air outbreaks, Bull. Am. Meteorol. Soc., 103, E1371–E1389, https://doi.org/10.1175/BAMS-D-21-0044.1, 2022.

Hofer, S., Hahn, L. C., Shaw, J. K., McGraw, Z. S., Bruno, O., Hellmuth, F., Pietschnig, M., Mostue, I. A., David, R. O., Carlsen, T., and Storelvmo, T.: Realistic representation of mixed-phase clouds increases projected climate warming, Commun. Earth Environ., 5, 390, https://doi.org/10.1038/s43247-024-01524-2, 2024.

Houze, R. A. Jr., Rasmussen, K. L., Zuluaga, M. D., and Brodzik, S. R.: The variable nature of convection in the tropics and subtropics: A legacy of 16 years of the Tropical Rainfall Measuring Mission satellite, Rev. Geophys., 53, 994–1021, https://doi.org/10.1002/2015RG000488, 2015.

Hu, Y., Rodier, S., Xu, K.-M., Sun, W., Huang, J., Lin, B., Zhai, P., and Josset, D.: Occurrence, liquid water content, and fraction of supercooled water clouds from combined CALIOP/IIR/MODIS measurements, J. Geophys. Res.-Atmos., 115, D00H34, https://doi.org/10.1029/2009JD012384, 2010.

Illingworth, A. J., Barker, H. W., Beljaars, A., Ceccaldi, M., Chepfer, H., Clerbaux, N., Cole, J., Delanoë, J., Domenech, C., Donovan, D. P., Fukuda, S., Hirakata, M., Hogan, R. J., Hünerbein, A., Kollias, P., Kubota, T., Nakajima, T., Nakajima, T. Y., Nishizawa, T., Ohno, Y., Okamoto, H., Oki, R., Sato, K., Satoh, M., Shephard, M. W., Velázquez-Blázquez, A., Wandinger, U., Wehr, T., and van Zadelhoff, G.-J.: The EarthCARE satellite: The next step forward in global measurements of clouds, aerosols, precipitation, and radiation, Bull. Am. Meteorol. Soc., 96, 1311–1332, https://doi.org/10.1175/BAMS-D-12-00227.1, 2015.

Irbah, A., Delanoë, J., van Zadelhoff, G.-J., Donovan, D. P., Kollias, P., Puigdomènech Treserras, B., Mason, S., Hogan, R. J., and Tatarevic, A.: The classification of atmospheric hydrometeors and aerosols from the EarthCARE radar and lidar: The A-TC, C-TC and AC-TC products, Atmos. Meas. Tech., 16, 2795–2820, https://doi.org/10.5194/amt-16-2795-2023, 2023.

Japan Aerospace Exploration Agency (JAXA): Release notes for the EarthCARE/CPR Level-1b Product, Tech. Rep. SEC-2024057 Rev.C, Japan Aerospace Exploration Agency (JAXA), https://www.eorc.jaxa.jp/EARTHCARE/document/L1ProductList/ReleaseNote/CPR/SEC-2024057-0C_Release_Notes_for_EarthCARE_CPR_L1b_Product.pdf, (last access: 14 August 2026), 2025.

https://doi.org/10.5194/egusphere-2026-6312
Preprint. Discussion started: 23 October 2026
© Author(s) 2026. CC BY 4.0 License.

Jensen, A. A., Harrington, J. Y., Morrison, H., and Milbrandt, J. A.: Predicting ice shape evolution in a bulk microphysics model, J. Atmos. Sci., 74, 2081–2104, https://doi.org/10.1175/JAS-D-16-0350.1, 2017.

Kalesse, H. and Kollias, P.: Climatology of high cloud dynamics using profiling ARM Doppler radar observations, J. Clim., 26, 6340–6359, https://doi.org/10.1175/JCLI-D-12-00695.1, 2013.

Kalesse, H., Szyrmer, W., Kneifel, S., Kollias, P., and Luke, E.: Fingerprints of a riming event on cloud radar Doppler spectra: observations and modeling, Atmos. Chem. Phys., 16, 2997–3012, https://doi.org/10.5194/acp-16-2997-2016, 2016.

Kalogeras, P., Battaglia, A., and Kollias, P.: Supercooled liquid water detection capabilities from Ka-band Doppler profiling radars: Moment-based algorithm formulation and assessment, Remote Sens., 13, 2891, https://doi.org/10.3390/rs13152891, 2021.

Karalis, M., Sotiropoulou, G., Abel, S. J., Bossioli, E., Georgakaki, P., Methymaki, G., Nenes, A., and Tombrou, M.: Effects of secondary ice processes on a stratocumulus to cumulus transition during a cold-air outbreak, Atmos. Res., 277, 106 302, https://doi.org/10.1016/j.atmosres.2022.106302, 2022.

Karrer, M., Seifert, A., Siewert, C., Ori, D., von Lerber, A., and Kneifel, S.: Ice particle properties inferred from aggregation modelling, J. Adv. Model. Earth Syst., 12, e2020MS002 066, https://doi.org/10.1029/2020MS002066, 2020.

Kim, J., Kollias, P., Puigdomènech Treserras, B., Battaglia, A., and Tan, I.: Evaluation of the EarthCARE Cloud Profiling Radar (CPR) Doppler velocity measurements using surface-based observations, Atmos. Chem. Phys., 25, 15 389–15 402, https://doi.org/10.5194/acp-25-15389-2025, 2025.

Kim, J., Tan, I., Kollias, P., and Puigdomènech Treserras, B.: First EarthCARE CPR observations of dynamics–microphysics coupling in marine cold-air outbreak clouds, Geophys. Res. Lett., 53, e2025GL121 514, https://doi.org/10.1029/2025GL121514, 2026.

Klein, S. A., McCoy, R. B., Morrison, H., Ackerman, A. S., Avramov, A., de Boer, G., Chen, M., Cole, J. N. S., Del Genio, A. D., Falk, M., Foster, M. J., Fridlind, A. M., Golaz, J.-C., Hashino, T., Harrington, J. Y., Hoose, C., Khairoutdinov, M. F., Larson, V. E., Liu, X., Luo, Y., McFarquhar, G. M., Menon, S., Neggers, R. A. J., Park, S., Poellot, M. R., von Salzen, K., Schmidt, G. M., Sednev, I., Shipway, B. J., Shupe, M. D., Spangenberg, D. A., Sud, Y. C., Turner, D. D., Veron, D. E., Walker, G. K., Wang, Z., Wolf, A. B., Xie, S., Xu, K.-M., Yang, F., and Zhang, G. J.: Intercomparison of model simulations of mixed-phase clouds observed during the ARM Mixed-Phase Arctic Cloud Experiment. I: Single-layer cloud, Q. J. R. Meteorol. Soc., 135, 979–1002, https://doi.org/10.1002/qj.416, 2009.

Kneifel, S. and Moisseev, D.: Long-term statistics of riming in nonconvective clouds derived from ground-based Doppler cloud radar observations, J. Atmos. Sci., 77, 3495–3508, https://doi.org/10.1175/JAS-D-20-0007.1, 2020.

Kneifel, S., von Lerber, A., Tiira, J., Moisseev, D., Kollias, P., and Leinonen, J.: Observed relations between snowfall microphysics and triple-frequency radar measurements, J. Geophys. Res.-Atmos., 120, 6034–6055, https://doi.org/10.1002/2015JD023156, 2015.

https://doi.org/10.5194/egusphere-2026-6312
Preprint. Discussion started: 23 October 2026
© Author(s) 2026. CC BY 4.0 License.

Kneifel, S., Kollias, P., Battaglia, A., Leinonen, J., Maahn, M., Kalesse, H., and Tridon, F.: First observations of triple-frequency radar Doppler spectra in snowfall: Interpretation and applications, Geophys. Res. Lett., 43, 2225–2233, https://doi.org/10.1002/2015GL067618, 2016.

Kollias, P., Battaglia, A., Tatarevic, A., Lamer, K., Tridon, F., and Pfitzenmaier, L.: The EarthCARE cloud profiling radar (CPR) Doppler measurements in deep convection: Challenges, post-processing, and science applications, in: Remote Sensing of the Atmosphere, Clouds, and Precipitation VII, edited by Im, E. and Yang, S., vol. 10776, pp. 57–68, SPIE, https://doi.org/10.1117/12.2324321, 2018.

Kollias, P., Battaglia, A., Lamer, K., Puigdomènech Treserras, B., and Braun, S. A.: Mind the gap–Part 3: Doppler velocity measurements from space, Front. Remote Sens., 3, 860 284, https://doi.org/10.3389/frsen.2022.860284, 2022.

Kollias, P., Puigdomènech Treserras, B., Battaglia, A., Borque, P. C., and Tatarevic, A.: Processing reflectivity and Doppler velocity from EarthCARE's cloud-profiling radar: The C-FMR, C-CD and C-APC products, Atmos. Meas. Tech., 16, 1901–1914, https://doi.org/10.5194/amt-16-1901-2023, 2023.

Korolev, A.: Limitations of the Wegener–Bergeron–Findeisen mechanism in the evolution of mixed-phase clouds, J. Atmos. Sci., 64, 3372– 3375, https://doi.org/10.1175/JAS4035.1, 2007.

Korolev, A. and Field, P. R.: The effect of dynamics on mixed-phase clouds: Theoretical considerations, J. Atmos. Sci., 65, 66–86, https://doi.org/10.1175/2007JAS2355.1, 2008.

Korolev, A. and Milbrandt, J.: How are mixed-phase clouds mixed?, Geophys. Res. Lett., 49, e2022GL099 578, https://doi.org/10.1029/2022GL099578, 2022.

Korolev, A., McFarquhar, G., Field, P. R., Franklin, C., Lawson, P., Wang, Z., Williams, E., Abel, S. J., Axisa, D., Borrmann, S., Crosier, J., Fugal, J., Krämer, M., Lohmann, U., Schlenczek, O., Schnaiter, M., and Wendisch, M.: Mixed-phase clouds: Progress and challenges, Meteorol. Monogr., 58, 5.1–5.50, https://doi.org/10.1175/AMSMONOGRAPHS-D-17-0001.1, 2017.

Korolev, A. V. and Mazin, I. P.: Supersaturation of water vapor in clouds, J. Atmos. Sci., 60, 2957–2974, https://doi.org/10.1175/1520-0469(2003)060<2957:SOWVIC>2.0.CO;2, 2003.

Korolev, A. V., Strapp, J. W., Isaac, G. A., and Nevzorov, A. N.: The Nevzorov airborne hot-wire LWC–TWC probe: Principle of operation and performance characteristics, J. Atmos. Ocean. Technol., 15, 1495–1510, https://doi.org/10.1175/1520-0426(1998)015<1495:TNAHWL>2.0.CO;2, 1998.

Kötsche, A., Maahn, M., Ettrichrätz, V., and Kalesse-Los, H.: Snow microphysical processes in orographic turbulence revealed by cloud radar and in situ snowfall camera observations, Atmos. Chem. Phys., 26, 3277–3297, https://doi.org/10.5194/acp-26-3277-2026, 2026.

Lawson, R. P., Baker, B. A., Schmitt, C. G., and Jensen, T. L.: An overview of microphysical properties of Arctic clouds observed in May and July 1998 during FIRE ACE, J. Geophys. Res.-Atmos., 106, 14 989–15 014, https://doi.org/10.1029/2000JD900789, 2001.

Leinonen, J. and Szyrmer, W.: Radar signatures of snowflake riming: A modeling study, Earth Space Sci., 2, 346–358, https://doi.org/10.1002/2015EA000102, 2015.

https://doi.org/10.5194/egusphere-2026-6312
Preprint. Discussion started: 23 October 2026
© Author(s) 2026. CC BY 4.0 License.

Leinonen, J., Lebsock, M. D., Tanelli, S., Sy, O. O., Dolan, B., Chase, R. J., Finlon, J. A., von Lerber, A., and Moisseev, D.: Retrieval of snowflake microphysical properties from multifrequency radar observations, Atmos. Meas. Tech., 11, 5471–5488, https://doi.org/10.5194/amt-11-5471-2018, 2018.

Li, Y. and Gu, H.: Relationship between middle stratiform clouds and large scale circulation over eastern China, Geophys. Res. Lett., 33, L09 706, https://doi.org/10.1029/2005GL025615, 2006.

Locatelli, J. D. and Hobbs, P. V.: Fall speeds and masses of solid precipitation particles, J. Geophys. Res., 79, 2185–2197, https://doi.org/10.1029/JC079i015p02185, 1974.

Luke, E. P., Kollias, P., and Shupe, M. D.: Detection of supercooled liquid in mixed-phase clouds using radar Doppler spectra, J. Geophys. Res.-Atmos., 115, D19 201, https://doi.org/10.1029/2009JD012884, 2010.

Mammatt, R. M., Westbrook, C., and McCusker, K.: Characterising the occurrence of monomodal and multimodal ice hydrometeor populations and their fall speeds in midlatitude frontal ice clouds using radar Doppler spectra, EGUsphere, https://doi.org/10.5194/egusphere-2026-2928, 2026.

Mason, S. L., Chiu, C. J., Hogan, R. J., Moisseev, D., and Kneifel, S.: Retrievals of riming and snow density from vertically pointing Doppler radars, J. Geophys. Res.-Atmos., 123, 13 807–13 834, https://doi.org/10.1029/2018JD028603, 2018.

Matrosov, S. Y.: Frozen hydrometeor terminal fall velocity dependence on particle habit and riming as observed by vertically pointing radars, J. Appl. Meteorol. Climatol., 62, 1023–1038, https://doi.org/10.1175/JAMC-D-23-0002.1, 2023.

Morrison, H. and Milbrandt, J. A.: Parameterization of cloud microphysics based on the prediction of bulk ice particle properties. Part I: Scheme description and idealized tests, J. Atmos. Sci., 72, 287–311, https://doi.org/10.1175/JAS-D-14-0065.1, 2015.

Morrison, H., de Boer, G., Feingold, G., Harrington, J., Shupe, M. D., and Sulia, K.: Resilience of persistent Arctic mixed-phase clouds, Nat. Geosci., 5, 11–17, https://doi.org/10.1038/ngeo1332, 2012.

Morrison, H., Milbrandt, J. A., Bryan, G. H., Ikeda, K., Tessendorf, S. A., and Thompson, G.: Parameterization of cloud microphysics based on the prediction of bulk ice particle properties. Part II: Case study comparisons with observations and other schemes, J. Atmos. Sci., 72, 312–339, https://doi.org/10.1175/JAS-D-14-0066.1, 2015.

Morrison, H., van Lier-Walqui, M., Fridlind, A. M., Grabowski, W. W., Harrington, J. Y., Hoose, C., Korolev, A., Kumjian, M. R., Milbrandt, J. A., Pawlowska, H., Posselt, D. J., Prat, O. P., Reimel, K. J., Shima, S.-I., van Diedenhoven, B., and Xue, L.: Confronting the challenge of modeling cloud and precipitation microphysics, J. Adv. Model. Earth Syst., 12, e2019MS001689, https://doi.org/10.1029/2019MS001689, 2020.

Mosimann, L.: An improved method for determining the degree of snow crystal riming by vertical Doppler radar, Atmos. Res., 37, 305–323, https://doi.org/10.1016/0169-8095(94)00050-N, 1995.

Mosimann, L., Weingartner, E., and Waldvogel, A.: An analysis of accreted drop sizes and mass on rimed snow crystals, J. Atmos. Sci., 51, 1548–1558, https://doi.org/10.1175/1520-0469(1994)051<1548:AAOADS>2.0.CO;2, 1994.

https://doi.org/10.5194/egusphere-2026-6312
Preprint. Discussion started: 23 October 2026
© Author(s) 2026. CC BY 4.0 License.

Nguyen, C. M., Wolde, M., Battaglia, A., Nichman, L., Bliankinshtein, N., Haimov, S., Bala, K., and Schuettemeyer, D.: Coincident in situ and triple-frequency radar airborne observations in the Arctic, Atmos. Meas. Tech., 15, 775–795, https://doi.org/10.5194/amt-15-775-2022, 2022.

Ockenfuß, P., Gergely, M., Frech, M., and Kneifel, S.: Spatial and temporal scales of riming events in nonconvective clouds derived from long-term cloud radar observations in Germany, J. Geophys. Res.-Atmos., 130, e2024JD042 180, https://doi.org/10.1029/2024JD042180, 2025.

Ono, A.: The shape and riming properties of ice crystals in natural clouds, J. Atmos. Sci., 26, 138–147, https://doi.org/10.1175/1520-0469(1969)026<0138:TSARPO>2.0.CO;2, 1969.

Oue, M., Kollias, P., Matrosov, S. Y., Battaglia, A., and Ryzhkov, A. V.: Analysis of the microphysical properties of snowfall using scanning polarimetric and vertically pointing multi-frequency Doppler radars, Atmos. Meas. Tech., 14, 4893–4913, https://doi.org/10.5194/amt-14-4893-2021, 2021.

Plana-Fattori, A., Protat, A., and Delanoë, J.: Observing ice clouds with a Doppler cloud radar, C. R. Phys., 11, 96–103, https://doi.org/10.1016/j.crhy.2009.11.004, 2010.

Planat, N., Gehring, J., Vignon, É., and Berne, A.: Identification of snowfall microphysical processes from Eulerian vertical gradients of polarimetric radar variables, Atmos. Meas. Tech., 14, 4543–4564, https://doi.org/10.5194/amt-14-4543-2021, 2021.

Praz, C., Roulet, Y.-A., and Berne, A.: Solid hydrometeor classification and riming degree estimation from pictures collected with a Multi-Angle Snowflake Camera, Atmos. Meas. Tech., 10, 1335–1357, https://doi.org/10.5194/amt-10-1335-2017, 2017.

Protat, A. and Williams, C. R.: The accuracy of radar estimates of ice terminal fall speed from vertically pointing Doppler radar measurements, J. Appl. Meteorol. Climatol., 50, 2120–2138, https://doi.org/10.1175/JAMC-D-10-05031.1, 2011.

Puigdomènech Treserras, B., Kollias, P., Battaglia, A., Tanelli, S., and Nakatsuka, H.: EarthCARE's cloud profiling radar antenna pointing correction using surface Doppler measurements, Atmos. Meas. Tech., 18, 5607–5618, https://doi.org/10.5194/amt-18-5607-2025, 2025.

Puigdomènech Treserras, B., Kollias, P., and Battaglia, A.: Retrieval and climatology of hydrometeor sedimentation velocity from EarthCARE Cloud Profiling Radar observations, 2026. (manuscript in preparation)

Qu, Z., Nguyen, C., Borque, P., Korolev, A., Barker, H. W., Ranjbar, K., Liu, L., Mariani, Z., Kacimi, M., Cholette, M., Heckman, I., et al.: EarthCARE Commissioning Calibration and Validation Campaign in Ottawa (ECALOT): An integrated approach to multi-level EarthCARE validation, EGUsphere, https://doi.org/10.5194/egusphere-2026-5347, 2026.

Sasikumar, S., Battaglia, A., Puigdomènech Treserras, B., and Kollias, P.: The estimation of path integrated attenuation for the EarthCARE cloud profiling radar, Atmos. Meas. Tech., 19, 2313–2328, https://doi.org/10.5194/amt-19-2313-2026, 2026.

Schrom, R. S. and Kumjian, M. R.: Connecting microphysical processes in Colorado winter storms with vertical profiles of radar observations, J. Appl. Meteorol. Climatol., 55, 1771–1787, https://doi.org/10.1175/JAMC-D-15-0338.1, 2016.

https://doi.org/10.5194/egusphere-2026-6312
Preprint. Discussion started: 23 October 2026
© Author(s) 2026. CC BY 4.0 License.

Shupe, M. D., Kollias, P., Matrosov, S. Y., and Schneider, T. L.: Deriving mixed-phase cloud properties from Doppler radar spectra, J. Atmos. Ocean. Tech., 21, 660–670, https://doi.org/10.1175/1520-0426(2004)021<0660:DMCPFD>2.0.CO;2, 2004.

Shupe, M. D., Daniel, J. S., de Boer, G., Eloranta, E. W., Kollias, P., Long, C. N., Luke, E. P., Turner, D. D., and Verlinde, J.: A focus on mixed-phase clouds: The status of ground-based observational methods, Bull. Am. Meteorol. Soc., 89, 1549–1562, https://doi.org/10.1175/2008BAMS2378.1, 2008.

Tornow, F., Ackerman, A. S., and Fridlind, A. M.: Preconditioning of overcast-to-broken cloud transitions by riming in marine cold air outbreaks, Atmos. Chem. Phys., 21, 12 049–12 067, https://doi.org/10.5194/acp-21-12049-2021, 2021.

Tridon, F., Battaglia, A., and Kneifel, S.: Estimating total attenuation using Rayleigh targets at cloud top: Applications in multilayer and mixed-phase clouds observed by ground-based multifrequency radars, Atmos. Meas. Tech., 13, 5065–5085, https://doi.org/10.5194/amt-13-5065-2020, 2020.

Tridon, F., Silber, I., Battaglia, A., Kneifel, S., Fridlind, A., Kalogeras, P., and Dhillon, R.: Highly supercooled riming and unusual triple-frequency radar signatures over McMurdo Station, Antarctica, Atmos. Chem. Phys., 22, 12 467–12 491, https://doi.org/10.5194/acp-22-12467-2022, 2022.

Turner, D. D., Kneifel, S., and Cadeddu, M. P.: An improved liquid water absorption model at microwave frequencies for supercooled liquid water clouds, J. Atmos. Ocean. Technol., 33, 33–44, https://doi.org/10.1175/JTECH-D-15-0074.1, 2016.

Vogl, T., Maahn, M., Kneifel, S., Schimmel, W., Moisseev, D., and Kalesse-Los, H.: Using artificial neural networks to predict riming from Doppler cloud radar observations, Atmos. Meas. Tech., 15, 365–381, https://doi.org/10.5194/amt-15-365-2022, 2022.

von Terzi, L., Dias Neto, J., Ori, D., Myagkov, A., and Kneifel, S.: Ice microphysical processes in the dendritic growth layer: A statistical analysis combining multi-frequency and polarimetric Doppler cloud radar observations, Atmos. Chem. Phys., 22, 11 795–11 821, https://doi.org/10.5194/acp-22-11795-2022, 2022.

Waitz, F., Schnaiter, M., Leisner, T., and Järvinen, E.: In situ observation of riming in mixed-phase clouds using the PHIPS probe, Atmos. Chem. Phys., 22, 7087–7103, https://doi.org/10.5194/acp-22-7087-2022, 2022.

Wegener, A.: Thermodynamik der Atmosphäre, Johann Ambrosius Barth, Leipzig, 1911.

Wehr, T., Kubota, T., Tzeremes, G., Wallace, K., Nakatsuka, H., Ohno, Y., Koopman, R., Rusli, S., Kikuchi, M., Eisinger, M., Tanaka, T., Taga, M., Deghaye, P., Tomita, E., and Bernaerts, D.: The EarthCARE mission–science and system overview, Atmos. Meas. Tech., 16, 3581–3608, https://doi.org/10.5194/amt-16-3581-2023, 2023.

Weiss, R. R. and Hobbs, P. V.: The use of a vertically pointing pulsed Doppler radar in cloud physics and weather modification studies, J. Appl. Meteorol., 14, 222–231, https://doi.org/10.1175/1520-0450(1975)014<0222:TUOAVP>2.0.CO;2, 1975.

Wilks, D. S.: Statistical Methods in the Atmospheric Sciences, vol. 100 of International Geophysics, Academic Press, 3 edn., ISBN 9780123850225, 2011.

Wolde, M., Battaglia, A., Nguyen, C., Pazmany, A. L., and Illingworth, A.: Implementation of polarization diversity pulse-pair technique using airborne W-band radar, Atmos. Meas. Tech., 12, 253–269, https://doi.org/10.5194/amt-12-253-2019, 2019.

https://doi.org/10.5194/egusphere-2026-6312
Preprint. Discussion started: 23 October 2026
© Author(s) 2026. CC BY 4.0 License.

Xu, Z., Kollias, P., Sasikumar, S., Battaglia, A., Puigdomènech Treserras, B., and McLinden, M. L. W.: EarthCARE Cloud Profiling Radar observations of the vertical structure of marine stratocumulus clouds, Atmos. Chem. Phys., 26, 4619–4632, https://doi.org/10.5194/acp-26-4619-2026, 2026.

Yan, J., Oue, M., Kollias, P., Luke, E., and Yang, F.: A radar view of ice microphysics and turbulence in Arctic cloud systems, Atmos. Chem. Phys., 25, 16 479–16 490, https://doi.org/10.5194/acp-25-16479-2025, 2025.

Zaremba, T. J. and Rauber, R. M.: The use of vertical gradients of radar reflectivity factor and radial velocity to diagnose dynamical and microphysical structures in extratropical cyclones: Results from IMPACTS, J. Atmos. Ocean. Technol., 42, 187–206, https://doi.org/10.1175/JTECH-D-24-0016.1, 2025.

Zhang, Y., Yu, R., Li, J., Yuan, W., and Zhang, M.: Dynamic and thermodynamic relations of distinctive stratus clouds on the lee side of the Tibetan Plateau in the cold season, J. Clim., 26, 8378–8391, https://doi.org/10.1175/JCLI-D-12-00636.1, 2013.